ACS APPLIED NANO MATERIALS

www.acsanm.org Review

Magnetic Particle Spectroscopy: A Short Review of Applications Using Magnetic Nanoparticles

Kai Wu,* Diqing Su, Renata Saha, Jinming Liu, Vinit Kumar Chugh, and Jian-Ping Wang*

Cite This: *ACS Appl. Nano Mater.* 2020, 3, 4972–4989 Read Online

ACCESS | Metrics & More | Article Recommendations

ABSTRACT: Magnetic particle spectroscopy (MPS), also called magnetization response spectroscopy (MRS), is a versatile measurement tool derived from magnetic particle imaging (MPI). It can be interpreted as a zero-dimensional MPI scanner. MPS was primarily designed for characterizing superparamagnetic iron oxide nanoparticles (SPIONs) regarding their applicability for MPI. In recent years, it has evolved into an independent, versatile, highly sensitive, inexpensive platform for biological and biomedical assays, cell labeling and tracking, and blood analysis. MPS has also developed into an auxiliary tool for magnetic imaging and hyperthermia by providing high spatial and temporal mappings of temperature and viscosity. Furthermore, other MPS-based applications are being explored such as magnetic fingerprints for target tracking and identification. There are a variety of MPS-based applications being reported and demonstrated by many groups. In this short review, we highlight some of the representative applications based on the MPS platform, thereby providing a roadmap of this technology and our insights for researchers in this area.

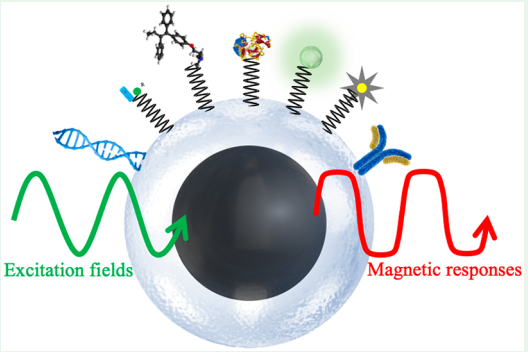

KEYWORDS: *magnetic particle spectroscopy, superparamagnetic iron oxide nanoparticles, magnetic particle imaging, bioassay, cell labeling and tracking*

1. INTRODUCTION

Magnetic particle spectroscopy (MPS) is a flourishing research area that closely relates to magnetic particle imaging (MPI). While MPI directly measures and maps the concentration of superparamagnetic iron oxide nanoparticles (SPIONs) over a spatial position, MPS is interpreted as a zero-dimensional MPI scanner that conducts spectroscopic studies on SPIONs. Although high-moment magnetic nanoparticles (MNPs) such as iron nanoparticles can provide higher magnetic signals than SPIONs of the same size and enhance the sensitivity, the biocompatibility of these types of high-moment MNPs needs to be further investigated.[1−8] Herein, in this work we only focus on the MPS-based applications using SPIONs. Primarily, the MPS platform was dedicated to assessing the performance of the SPION magnetic tracers regarding their applicability for MPI.[9−15] Over the years, it has developed into a highly sensitive, fast, and versatile sensing platform for a wide variety of biological and biomedical assays.[16−20] In MPS, sinusoidal magnetic fields are applied to periodically magnetize SPIONs. The magnetic moments of SPIONs tend to align with the applied fields through relaxation processes (Néel and Brownian processes), which are countered by thermal fluctuation. In addition, the relaxation processes are directly linked to physical conditions such as the viscosity and temperature of a SPION aqueous medium as well as the states of target analytes (chemicals/biological compounds) bound to the SPIONs.[18,19,21−31] On the other hand, SPIONs, with sizes comparable to those of chemical/biological compounds, have been the subject of increasing interest in the areas of medical diagnostics and therapy. In general, a SPION consists of a magnetic core (magnetite/maghemite) coated with inorganic and/or organic capping layers (e.g., dextran, chitosan, silica, etc.) to prevent aggregation and to improve the physicochemical stability under various physiological environments, as shown in Figure 1A. In addition, suitable surface functionalization of ligands/antibodies/aptamers/proteins onto SPIONs allows for highly selective chemical interactions with biological systems. Because of the negligible magnetic background from biological samples, highly sensitive detection could be achieved by using SPIONs as contrasts/markers/tracers.

In MPS, the dynamic magnetic responses of SPIONs, which contain unique higher odd harmonics, are harvested by a pair of pick-up coils. The MPS spectra (higher harmonic amplitude

Received: April 6, 2020
Accepted: May 5, 2020
Published: May 5, 2020

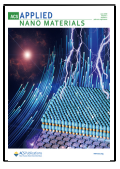

https://dx.doi.org/10.1021/acsanm.0c00890
ACS Appl. Nano Mater. 2020, 3, 4972–4989

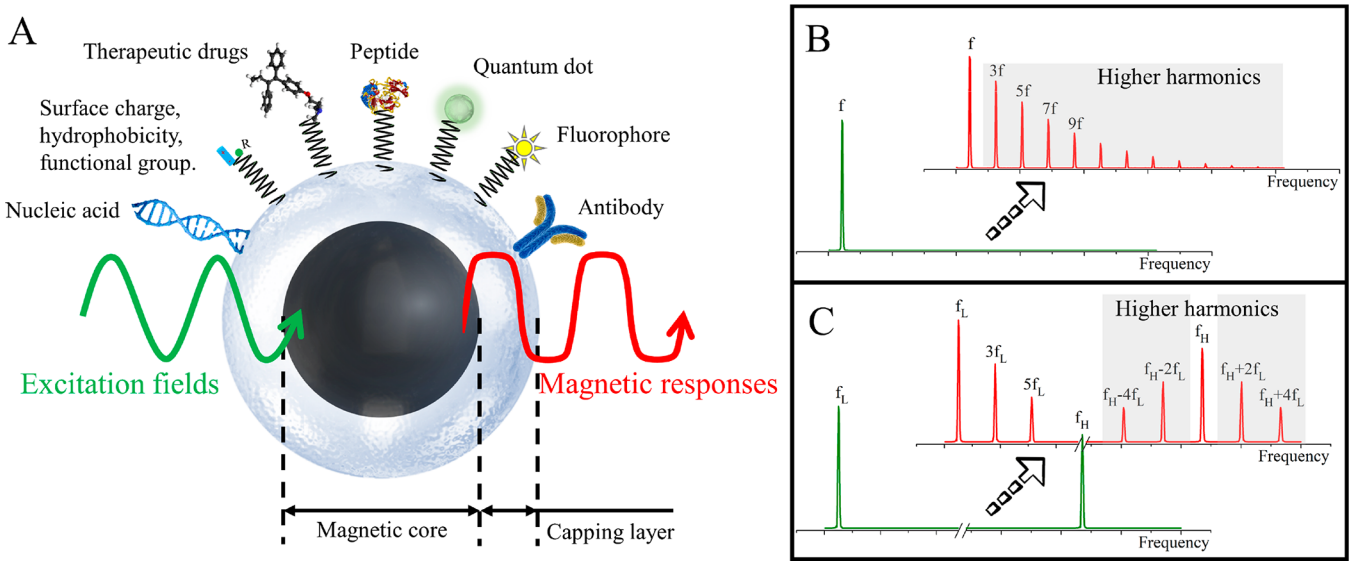

Figure 1. (A) Schematic drawing of a multifunctional SPION. Higher odd harmonics are generated by the dynamic magnetic responses of SPIONs under external excitation magnetic fields. (B) Spectrum of a monofrequency excitation field and the resulting MPS spectra. (C) Spectrum of a dual-frequency excitation field and the resulting MPS spectra.

and phase) are obtained by Fourier transform infrared of the detected time domain signal, as shown in Figure 1B,C. There are two type of MPS platforms reported in the literature: single and dual driving fields based MPS. In the single-driving-field-based MPS, one driving magnetic field with frequency f is applied to periodically magnetize the SPIONs.[18,26,32−37] Because of the nonlinear dynamic magnetic responses from SPIONs, higher odd harmonics at 3f (the third harmonic), 5f (the fifth harmonic), 7f (the seventh harmonic), etc., are harvested as metrics for different applications, as shown in Figure 1B. In the dual-driving-field-based MPS, one low-frequency field, f_L, with sufficiently large magnitude is applied to periodically magnetize the SPIONs, while the other high-frequency field, f_H, with small magnitude is applied to modulate the odd harmonics into the high-frequency range in order to reduce the $1/f$ noise.[30,30,31,38−42] Thus, the odd harmonics are found at $f_H \pm 2f_L$ (the third harmonics), $f_H \pm 4f_L$ (the fifth harmonics), $f_H \pm 6f_L$ (the seventh harmonics), etc., as shown in Figure 1C. These two MPS modalities have been theoretically studied, experimentally proven, and compared in many literatures. A variant of the MPS platform has also been reported by using one alternating magnetic field with low amplitude combined with a gradual direct-current (dc) offset.[43] Another review paper published by the authors has extensively explained the underlying theories of both MPS modalities as well as system setups. The literatures reporting their immunoassay applications before the year of 2016 were also covered, which can be found in ref 16. In this review, we will focus on the applications of MPS for immunoassays, cell and blood analysis, viscosity, temperature, and mechanical force monitoring, as well as magnetic fingerprint tools for target tracking and identification. Some representative literatures between the years 2015 and 2020 are also covered.

Because the harmonic amplitude is largely dependent on the quantity of SPIONs in the testing sample, the MPS results could be biased by deviations of the SPION quantities in each sample, especially for the scenarios of detecting very low abundancy of target analytes.[16] Because of this concern, other SPION quantity-independent metrics have been reported and demonstrated for bioassays, such as magnetic susceptibility, harmonic phase angle (or phase lag), and harmonic amplitude ratios (the third over the fifth harmonic ratio R35 or the fifth over the third harmonic ratio R53).[19,31,44−48] In recent years, MPS has shown a strong capability of sensing the subtle changes in any property influencing the Néel and/or Brownian processes of the SPIONs within seconds.

MPS bears superior advantages over conventional magnetometers by providing fast and simple measurement procedures for SPION systems without the need for cooling the device. The working mechanisms and theories of the MPS platform have been extensively reported by several papers.[9,16,20,49] Herein, in this review, we focus on the MPS-derived applications. We at first reviewed the MPS-based applications for biological and biomedical assays using surface-functionalized SPIONs as magnetic markers, followed by MPS-based cell analysis, where the SPIONs are used as contrast agents to monitor cell uptake, passage, and cell vitality.[19,31,35,37,50,51] Benefiting from the ease of surface-coating strategies (such as silica, polymer, dextran, etc.), nowadays, SPIONs with superior biocompatibility, biodegradability, and superparamagnetic nature are much desired magnetic markers/tracers for the aforementioned applications.[52−63] In addition, MPS has also been exploited as an auxiliary tool for applications such as magnetic imaging and hyperthermia by providing real-time viscosity and temperature mapping, as well as a mechanical force sensor in ball mills.[17,23,64,65] Furthermore, other MPS-based applications that are sometimes overlooked but own great market potential are characterization of SPIONs from an aqueous medium, marking/tracking of products in the complex global resource and supply chains, determination of the total blood volume, and evaluation of blood clot progression.[17,18,66−70] In this short review, we are only able to list some of the representative applications, and the MPS-based applications are not limited to this paper. We hope this review can provide insights into the great potential of MPS and serve as a roadmap for researchers in this area.

https://dx.doi.org/10.1021/acsanm.0c00890
ACS Appl. Nano Mater. 2020, 3, 4972−4989

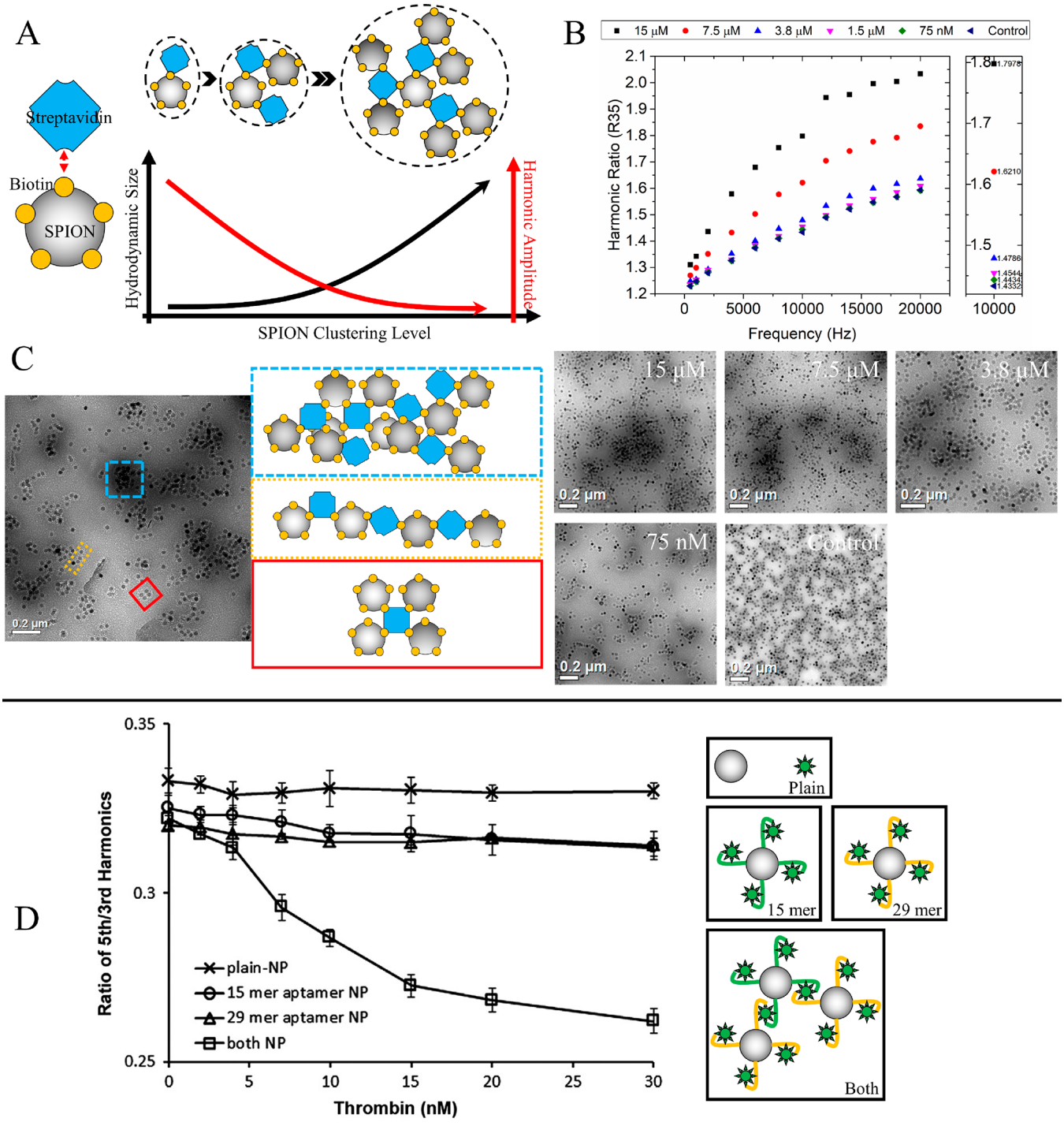

Figure 2. (A) Streptavidin- and biotin-functionalized SPIONs. As the quantity of streptavidin increases in the SPION liquid medium, the SPIONs are likely to form clusters. The dashed lines represent the hydrodynamic sizes of the SPIONs due to clustering. As the SPION clustering level increases, the hydrodynamic size increases and the harmonic amplitude decreases. (B) Harmonic ratio R35 collected from six SPION samples added with different concentrations (quantities) of streptavidin, plotted as a function of the driving-field frequency. The inset figure summarizes R35 under a driving-field frequency of 10 kHz. (C) Left: Bright-field TEM images of six SPION samples. Different SPION cluster models are given. Right: TEM images of SPION samples [15 μM, 7.5 μM, 3.8 μM, 75 nM, and control (0 nM)] showing that the degree of particle clustering increases as the quantity (concentration) of streptavidin increases. (D) Harmonic ratio R53 from two populations of SPIONs, conjugated with 15- and 29-mer antithrombin aptamers, as a function of the thrombin concentration. (A–C) Reprinted with permission from ref 31. Copyright 2019 American Chemical Society. (D) Reprinted with permission from ref 19. Copyright 2013 Elsevier.

2. MPS-BASED BIOLOGICAL AND BIOMEDICAL ASSAYS

2.1. MPS-Based Immunoassays. Following the discussion in the previous section, the magnetic moments of SPIONs relax to align with the external magnetic field through a joint Néel and Brownian process. The Néel process is the internal flipping of magnetic moment inside a stational SPION, while the Brownian process is the physical rotation of the entire SPION along with its magnetic moment. While both processes

https://dx.doi.org/10.1021/acsanm.0c00890
ACS Appl. Nano Mater. 2020, 3, 4972–4989

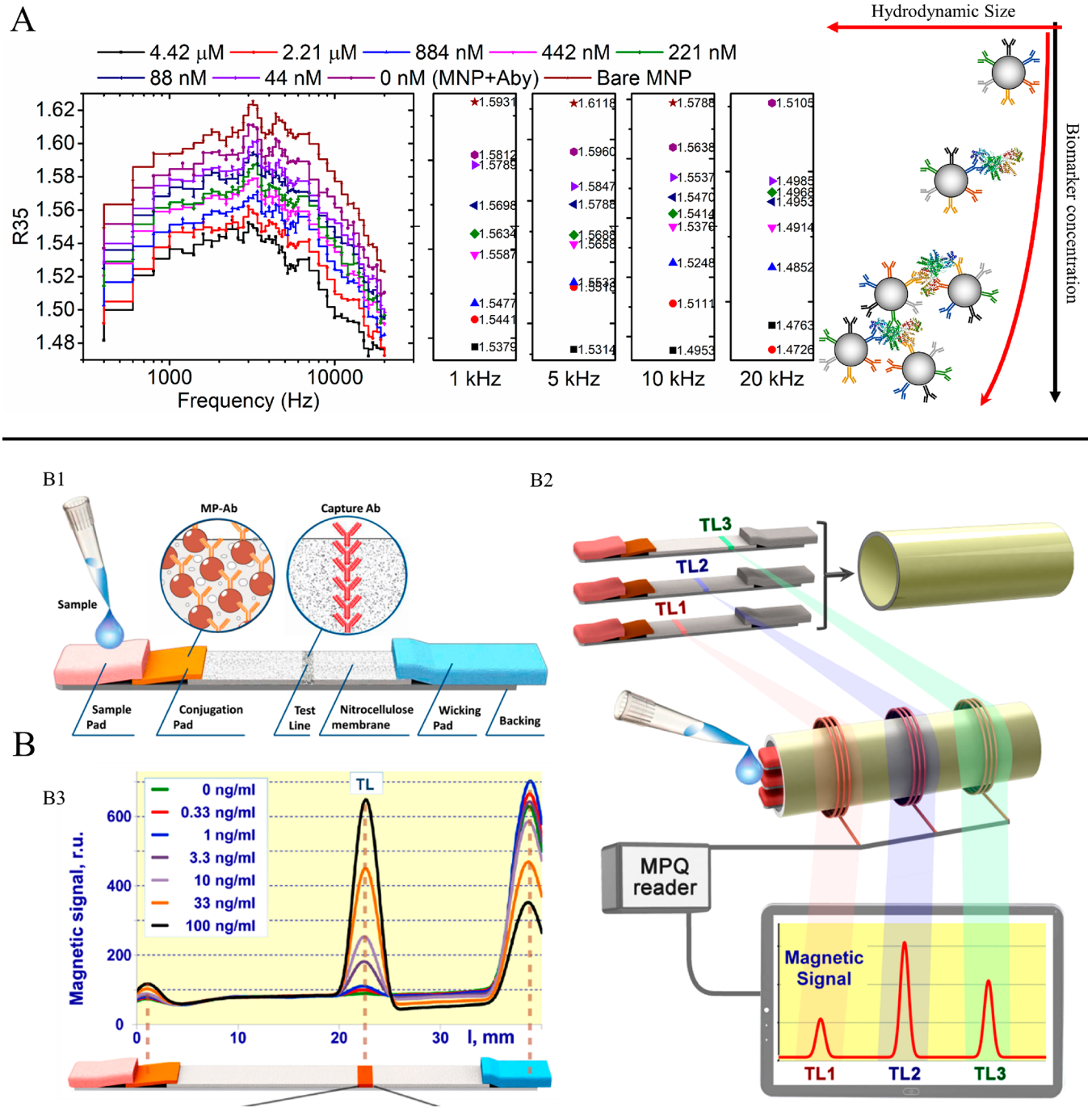

Figure 3. (A) Harmonic ratio R35 collected from nine SPION samples added with different concentrations (quantities) of H1N1 NP, plotted as a function of the driving-field frequency. Insets highlight the R35 measured at 1, 5, 10, and 20 kHz, respectively. (B) Multiplexed quantitative lateral flow assay. B1: Test strip design based on a sandwich-lateral flow assay with antibody-conjugated SPIONs as labels. B2: Multiplexed assay setup: several single-plex test strips with dissimilar positions of the test lines are combined in a miniature cartridge. The cartridge with a sample deposited onto its front end is inserted into the portable MPQ (also called MPS) reader. Simultaneous readout of magnetic signals from all participating test strips as seen at the bottom. (A) Reprinted with permission from ref 38. Copyright 2020 American Chemical Society. (B) Reprinted with permission from ref 90. Copyright 2016 American Chemical Society.

are countered by thermal fluctuation, the Néel process is also affected by the effective magnetic anisotropy (including magnetocrystalline anisotropy, shape anisotropy, surface anisotropy, etc.) and volume of the magnetic core. On the other hand, the Brownian process is affected by the liquid-medium viscosity and hydrodynamic volume of the SPION (volume of the magnetic core and surface attachments). For free and noninteracting SPIONs with magnetic core size below D_1, the Néel process guides the dynamic magnetic responses of SPIONs, while the Brownian process becomes the dominating factor when the magnetic core size of the SPION is above D_2 ($D_1 < D_2$). In addition, these values vary between different literatures and depend on several factors such as the effective magnetic anisotropy, medium viscosity and temperature, surface shell (organic and/or inorganic layers) thickness, etc.[39,66] For the applications of MPS-based immunoassays,

https://dx.doi.org/10.1021/acsanm.0c00890
ACS Appl. Nano Mater. 2020, 3, 4972−4989

Brownian-process-dominated SPIONs are most sensitive to the binding events of target analytes and, thus, are frequently used for this purpose. Sasayama et al. have systematically studied the effect of immobilization of SPIONs (where the Brownian process is blocked because of immobilization) on the alternating-current hysteresis loop and harmonics under different excitation magnetic field frequencies and amplitudes.[71] In addition, the magnetic core size distribution, alignment of easy axes, anisotropy of SPIONs, and driving-field frequency and amplitude can largely affect the harmonics.[72−77]

Herein, a streptavidin and biotin system with high binding affinity is at first demonstrated as the model system, as shown in Figure 2A.[31] Streptavidin is a crystalline tetrameric protein with a molecular weight of 4 × 15 kDa. SPIONs are surface-functionalized with biotins. Each streptavidin molecule can bind up to four biotins with high binding affinity, which allows interaction with multiple biotin moieties from different SPIONs and, as a result, forms SPION clusters. Six SPION samples are prepared, and each sample is added with streptavidin of different concentrations. The harmonic ratio R35 is plotted as a function of the driving-field frequency, which increases as the concentration/quantity of streptavidin increases, as shown in Figure 2B. Transmission electron microscopy (TEM) images are taken to investigate the SPION clusters in six samples. Well-dispersed SPIONs are observed from the negative control group (0 nM streptavidin), whereas bigger SPION clusters are observed from TEM images as the concentration of streptavidin increases, as shown in Figure 2C. In addition, different bound state models are presented. Because each tetrameric streptavidin hosts up to four biotin binding sites, SPIONs could form clusters, chains, tetramers, trimers, dimers, and so forth. In this kind of MPS-based immunoassay, SPION clustering (or agglomeration) caused by the target analyte can prolong the Brownian relaxation time significantly. Thus, the bound and freely rotating SPIONs are easily differentiated through the magnetic responses. Akiyoshi et al. and Enpuku et al. have reported this method for the detection of C-reactive proteins (CRPs).[78,79]

Zhang et al. reported a MPS-based bioassay using an aptamer−thrombin system.[19] Two antithrombin aptamers (15- and 29-mer) that can specifically bind to two different epitopes from thrombin are selected. Two groups of SPIONs are prepared, and each group is surface-functionalized with one type of antithrombin aptamer, as shown in Figure 2D. Each thrombin hosts two heterobinding domains that allows two SPIONs with different aptamers to bind with. Harmonic ratio R53 is collected as a SPION quantity-independent metric. Results show that adding a high concentration of thrombin to either the 15- or 29-mer aptamer-functionalized SPIONs alone produces a very limited change in the R35 metric. Larger R35 changes are observed in the presence of both groups of SPIONs, when 15- and 29-mer aptamers bind to heterobinding domains from thrombin, resulting in SPION clusters.

In December 2019, a novel strain of coronavirus belonging to the same family of viruses that cause severe acute respiratory syndrome (SARS) and Middle East respiratory syndrome (MERS) occurred in Wuhan, Hubei Province, China. Later, this causative virus has been named as severe acute respiratory syndrome coronavirus 2 (SARS-CoV-2), and the relevant infected disease has been named as coronavirus disease 2019 (COVID-19) by the World Health Organization. SARS-CoV-2 is an enveloped, positive-strand RNA virus with a large RNA genome of ∼30 kb.[80] The major structural proteins of coronavirus are spike (S), envelope (E), membrane (M), and nucleocapsid (N). Infection with the SARS-CoV-2 can be asymptomatic or can result in mild-to-severe symptomatic disease. There is currently no medication to treat COVID-19.[81−85] Testing for early detection of the virus is essential to slow down the spread of COVID-19 and for efficient implementation of control and containment strategies. Current diagnostic tests for COVID-19 are based on real-time reverse transcription polymerase-chain-reaction (RT-PCR) assays.[86−89] Although this test is sensitive, it requires expensive equipment, trained technicians to perform the test, and a turnaround time of at least 48 h. In addition, there are signs that the demand for PCR reagents may exceed supply during the current emergency. In view of this public health emergency, we added discussions reviewing MPS platforms for the detection of nucleic acids and protein biomarkers from viruses and pathogens.

Wu et al. reported a MPS-based bioassay design using a polyclonal antibody−antigen system for the quantitative detection of Influenza A Virus (IAV) subtype H1N1.[38] In their design, the MPS platform monitors the harmonics of SPIONs as a metric for the freedom of rotational process, which indicates the states of SPIONs bound to the target analyte. In order to artificially induce SPION clusters, IgG polyclonal antibodies are anchored onto SPION surfaces. The target analyte, H1N1 nucleoprotein (NP), hosts multiple different epitopes for these IgG polyclonal antibodies. In the presence of H1N1 NP, cross-linking takes place between SPIONs (IgG from the particle surface) and H1N1 NP, which forms SPION clusters, as shown in Figure 3A. Harmonic ratio R35 is collected, and this system is reported to detect as low as 44 nM (4.4 pmol) H1N1 NP. The feasibility of using MPS and target-analyte-induced SPION clustering provides a new direction for detecting ultralow concentrations of target analytes, which can be employed as a rapid, sensitive, and wash-free magnetic bioassay technique.

Orlov et al. reported a multiplexed quantitative lateral flow assay for the on-site detection of botulinum neurotoxin (BoNT) types A, B, and E from complex matrixes.[90] Multiplexing is achieved by a multichannel MPS technique [in their work, it is called a magnetic particle quantification (MPQ) technique]. As shown in Figure 3B (B1 and B2), three single-plex text strips (A-strip, B-strip, and E-strip) are combined in a cartridge. The assay procedures are the same as single-plex strip testing. The biofluid sample is dropped onto the front end of the cartridge, and then after ∼25 min, it is inserted into the three-channel MPS reader for measurements. The MPS reader records the magnetic responses from SPIONs within the measuring coils, as shown in Figure 3B (B3). This platform achieves the detection limits of 0.22, 0.11, and 0.32 ng/mL for BoNT-A, -B, and -E, respectively. The multiplexed bioassay performance has also been successfully validated by detecting BoNT from milk, apple, and orange juices. This developed multiplex assay can analyze media regardless of the optical properties and offers rapid, on-site, and sensitive detection.

It is already known that the binding events of target analytes affect the Brownian process and dynamic magnetic responses of SPIONs under external fields. While this detection mechanism yields detectable changes in the harmonic amplitudes, phases, and harmonic ratios, larger changes in these metrics can be achieved by designing multiple ligands/antibodies/aptamers/proteins on SPIONs that could bind to

https://dx.doi.org/10.1021/acsanm.0c00890
ACS Appl. Nano Mater. 2020, 3, 4972−4989

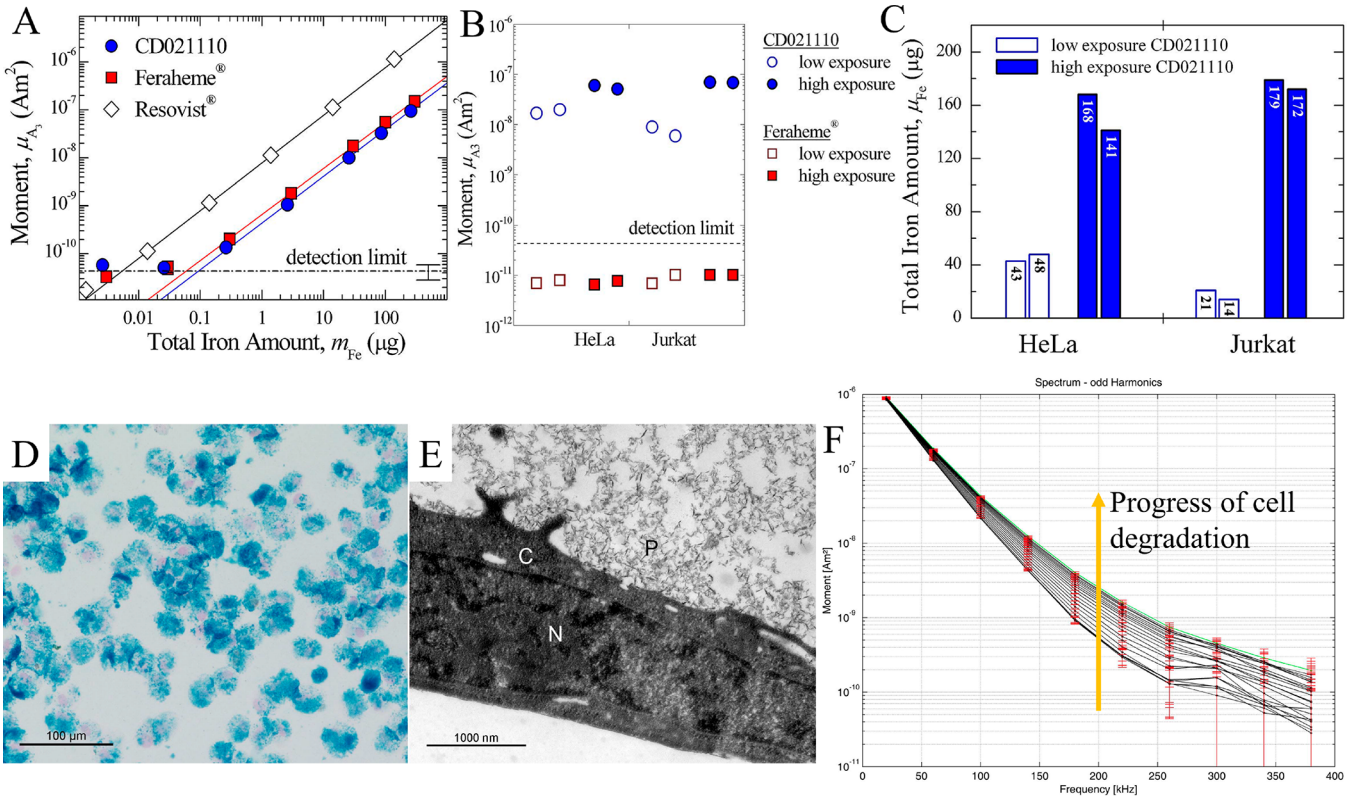

Figure 4. (A) Calibration curves of Feraheme, CD021110, and Resovist (a tracer most frequently used for MPI) SPIONs. (B) MPS signal (the third-harmonic amplitude) from harvested cells (HeLa and Jurkat) incubated with low and high concentrations of CD021110 and Feraheme SPIONs. (C) Cellular uptake of CD021110 SPIONs by HeLa and Jurkat cells quantified by MPS. The higher the dose of nanoparticles, the more the particles that have been resorbed by the cells. (D) Prussian blue staining that verifies the presence of SPIONs. Nuclei appear in light red. (E) TEM showing extracellular localization of SPIONs adhering to the cell's surface: C, cytoplasm; N, nucleus; P, SPIONs. (F) MPS spectra of degradation and degraded (gray/green line) stem cells measured at 20 kHz and 37 °C. The degradation process was continuously monitored. (A–C) Reprinted with permission from ref 35. Copyright 2012 IEEE. (D–F) Reprinted with permission from ref 51. Copyright 2015 IEEE.

heterobinding domains on the same biomarker, assembling the SPIONs into clusters or aggregates. This kind of detection mechanism greatly increased the hydrodynamic sizes of the SPIONs, resulting in increased relaxation time, which can be sensed by the MPS system.

Nonspecific binding (NSB) between other molecules/chemicals to the SPIONs is a critical problem in the design of MPS-based immunoassays because the purpose of MPS bioassays is to measure only the binding events between the target analytes and SPIONs, instead of the background. Some frequently used methods to prevent NSB are suggested herein as below: (1) adjust the pH of the SPION liquid medium; (2) use protein blockers such as bovine serum albumin to block spare binding sites on SPIONs; (3) use surfactants such as Tween 20 to disrupt hydrophobic interactions between target analytes and SPIONs; (4) adjust the salt concentration in the SPION liquid medium to prevent charges on the target analytes from interacting with charges on the SPIONs.

2.2. MPS-Based Cell Analysis. SPIONs have been used for a wide variety of applications such as molecular and cell separation, drug delivery, hyperthermia, magnetic resonance imaging (MRI), MPI, etc.[10,91−104] The need for quantitative methods to evaluate the SPION (or iron) content from contrast media solutions and biological matrixes is thus obvious. Various tools reported to measure the SPION (or iron) content such as spectrophotometric elemental analysis techniques (e.g., Perls' Prussian blue colorimetry), fluorophores/radionuclides-labeled SPIONs, and R1 relaxometry.[105−108] Despite the extensive work done to quantify iron in an aqueous matrix, these techniques suffer from an inability to distinguish between exogenous SPIONs and endogenous iron, a narrow detectable range, and nonlinearity.[35,105] Recently, MPS is reported as an alternative to measure the iron content (or to quantify SPIONs) from an aqueous matrix, where MPS utilizes the nonlinear magnetic responses from SPIONs exposed to an excitation magnetic field.

Loewa et al. reported the quantification of SPIONs uptaken in cells using a MPS platform,[35] where they took the third-harmonic amplitude as a measure for the SPION content. To this end, the harmonic amplitudes of known SPION (iron) content under the same excitation field condition are recorded. As shown in Figure 4A, the calibration curves are highly linear for all types of SPIONs. Two tumor cell lines, HeLa and Jurkat, were incubated with SPIONs of different concentrations, for 30 h, followed by the harvesting of ∼10^6 cells for MPS measurements. The third-harmonic amplitudes from these harvested cells are recorded in Figure 4B, indicating that the SPIONs were uptaken by cells. Using the calibration curves, the calculated iron content uptaken by cells is given in Figure 4C. Although this is a preliminary work without considering the impact of a SPION aqueous matrix (viscosity, binding, aggregations, etc.) and the influence of size-selective cellular uptake of SPIONs, this method provides the basis for the practical implementation of in vivo studies of the SPION (iron) content from tissue samples. Besides the harmonic amplitude, harmonic ratio R53 is also reported to be an

https://dx.doi.org/10.1021/acsanm.0c00890
ACS Appl. Nano Mater. 2020, 3, 4972−4989

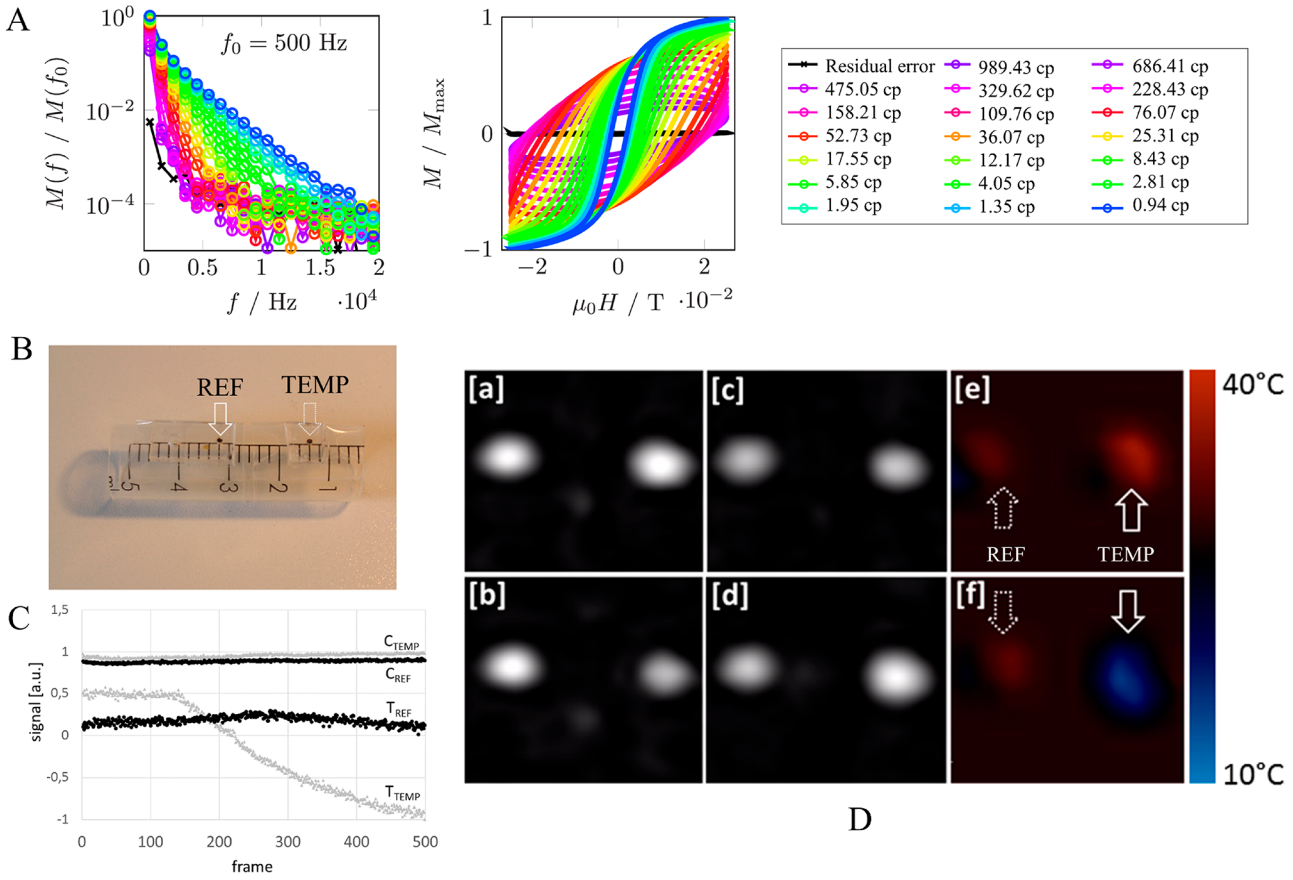

Figure 5. (A) Experimental results of the MPS harmonic amplitudes versus viscosity series acquired under a driving field of 500 Hz and 25 mT. The black lines represent the residual error R. Measurements were performed at room temperature T = 25 °C. (B) Plastic tube with two SPION samples. (C) Reconstructed MPI signals reflecting the amount of SPIONs (C_{TEMP} and C_{REF}) and temperature information (T_{TEMP} and T_{ERF}) of the tempered and reference probes. (D) Projection images of 3D reconstructed signal channels ([a]−[d]) and color-coded difference signals representing temperature ([e] and [f]) acquired at the beginning (top row) and end (bottom row) of the experiment. (A) Reprinted with permission from ref 17. Copyright 2019 American Chemical Society. (B−D) From ref 64; licensed under CC BY 4.0.

indicator to reveal distinct changes in the magnetic behavior of SPIONs in response to cellular uptake.[50]

Gräfe et al. established an in vitro testing system to investigate SPION transport across cellular layers as well as examine MPS for reliable SPION quantification.[37] A blood−brain barrier (BBB) representing a human brain microvascular endothelial cell (HBMEC) model was chosen. Their experiment confirms the excellent suitability of MPS for sensitive SPION quantification at different stages of particles passing cellular layers, indicating a promising future method to pass SPION-loaded drugs across a BBB without disturbing its integrity. As a result, the drug loading and release efficiency can be monitored by the MPS approach.

Fidler et al. reported MPS for in vitro cell vitality monitoring, where human mesenchymal stem cells (hMSCs) are labeled with SPIONs and tracked.[51] hMSCs are a promising tool in regenerative medicine and are able to repair damaged tissue. However, tissue healing using hMSCs will only be possible if cells can be homed to their target and are still vital. This challenge calls for a long-term, noninvasive method to label and monitor the cells. Fidler et al. labeled hMSCs with SPIONs, and the verification of SPION-labeled hMSCs by Prussian blue staining and TEM is shown in Figure 4D,E. For cell vitality assessment, the MPS spectra were continuously monitored during a cell degradation process initiated by adding sodium dodecyl (lauryl) sulfate (SDS; which dissolves the cells). As shown in Figure 4F, during dissolution of the cells by SDS, the MPS harmonic amplitudes increase and larger changes are observed from higher harmonics. The increase of the harmonic amplitudes can be attributed to a change in the Brownian relaxation, where, during the cell degradation process, cells are dissolved and SPIONs are released to a lower-viscosity extracellular environment (or from bound to unbound status). This work demonstrated the feasibility of using SPIONs with a MPS platform as reporters for cell homing and cell vitality, in an aqueous environment.

In summary, efficient noninvasive techniques for tracking cells in cell-based therapies and diagnostics are crucial. SPIONs, with superior biocompatible, biodegradable, and superparamagnetic nature, are much desired magnetic markers for labeling cells. Upon interaction with biological materials such as cells, SPIONs undergo physicochemical changes that alter their dynamic magnetic responses and eventually the MPS spectra.[50] Currently, there are many established techniques, including chromatographic and colorimetric iron assays and electron microscopy, that are not feasible with living cells. MPS may help to overcome these limitations.

3. MPS AS AN AUXILIARY TOOL

3.1. MPS for Viscosity and Temperature Monitoring.

The Brownian relaxation process is affected by the viscosity of the SPION liquid medium. Thus, this property has been

https://dx.doi.org/10.1021/acsanm.0c00890
ACS Appl. Nano Mater. 2020, 3, 4972−4989

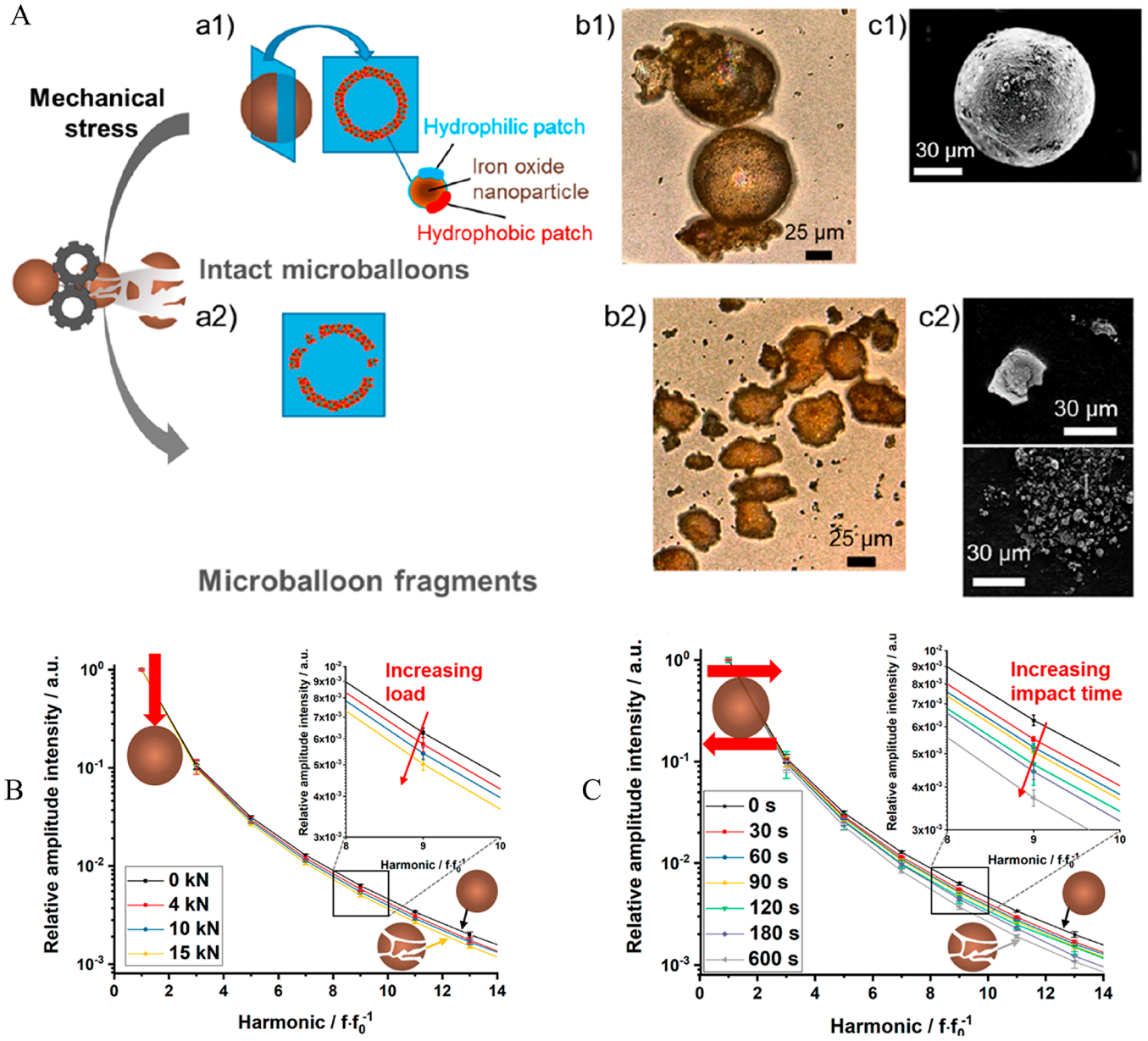

Figure 6. (A) Hollow microballoons composed of SPIONs. Drop of the MPS signal curves of microballoons during the application of quasi-static compression (B) or of dynamic shear and impact forces in a ball-mill-like setup (C), which increase significantly with increasing load or milling time, respectively. Reprinted with permission from ref 65. Copyright 2019 American Chemical Society.

applied for in vivo and in vitro viscosity monitoring using Brownian-process-dominated SPIONs.[17,22−24,109,110] As shown in Figure 5A, SPIONs are dispersed in different aqueous media of varying viscosities. At a driving-field frequency of 500 Hz, SPIONs from a low-viscosity medium show more higher harmonics and the slope of the harmonic curve increases as the viscosity increases. Under low-frequency excitation fields, magnetic moments of SPIONs can follow the field directions almost instantaneously via Brownian relaxation. The only countering force is the friction force from a high-viscosity medium. Therefore, there is a phase lag between magnetic moments (due to the slow response of the Brownian relaxation process) and the excitation field. The SPIONs do not reach equilibrium states before the excitation field changes direction. This relationship is reflected in the series of dynamic M−H curves in Figure 5A. Using this property of the Brownian relaxation process, Wu et al. proposed and demonstrated the feasibility of using MPS and SPIONs to measure the human serum viscosity in real time.[23] A standard calibration curve of third-harmonic amplitude versus viscosity was plotted for the estimation of any aqueous media with unknown viscosities.

In addition, the temperature information on the SPIONs' aqueous media can also be extracted from their magnetic responses because the Brownian relaxation process is also modulated by the temperature (thermal fluctuation). Several groups have reported the in vivo temperature measurements using MPS and SPIONs, where correlations between the temperature and Brownian relaxation time are obtained by measuring the MPS spectra (magnetic responses) across a range of frequencies and temperatures. Calibration curves are plotted to subsequently estimate the temperatures.[27,111,112]

In short, the temperature and viscosity information on the aqueous medium can be separated from the magnetic responses of SPIONs. In recent years, there are several

https://dx.doi.org/10.1021/acsanm.0c00890
ACS Appl. Nano Mater. 2020, 3, 4972−4989

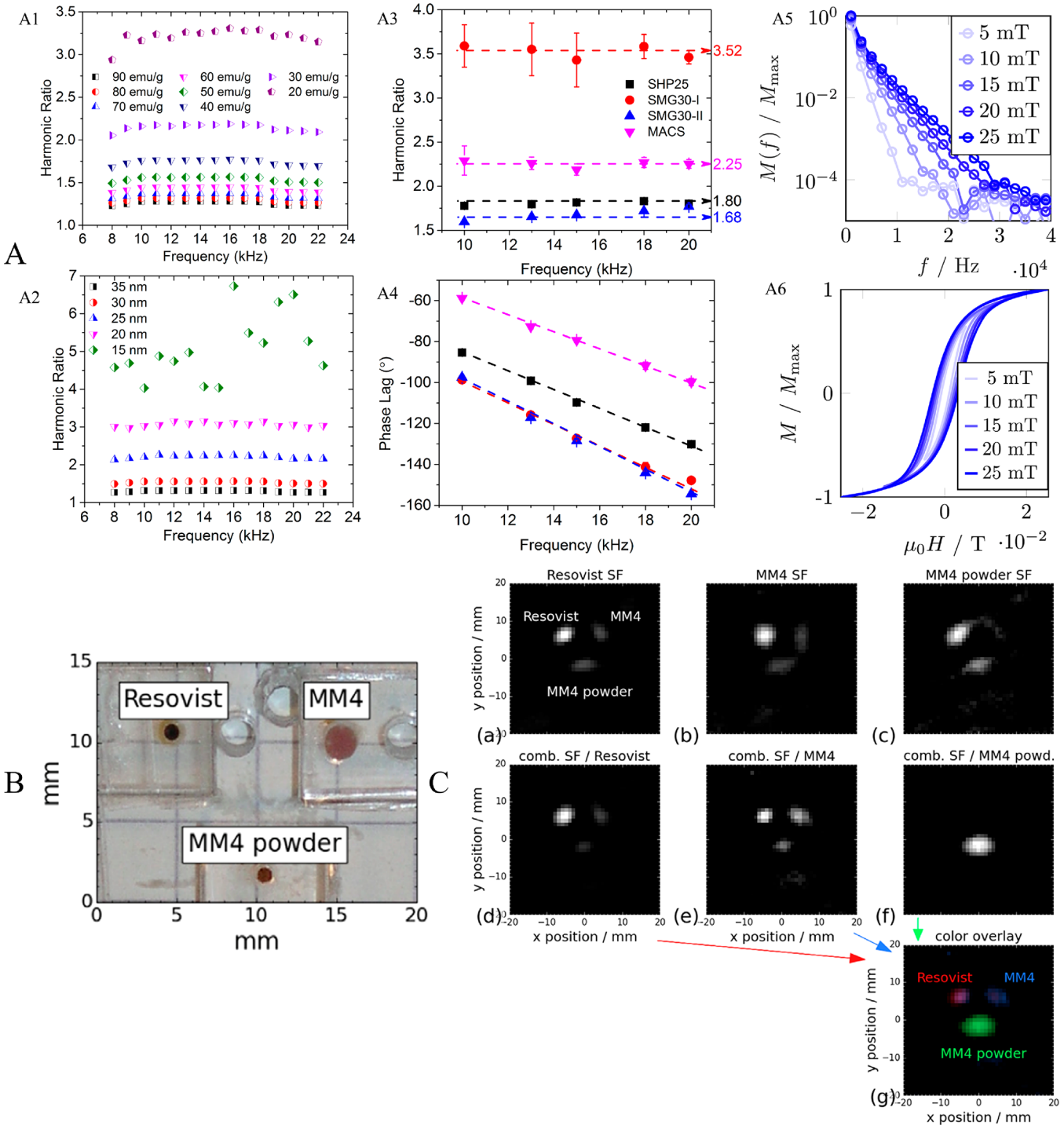

Figure 7. (A) MPS for SPION characterizations. A1: Simulated harmonic ratios R35 as a function of the excitation-field frequency when D = 30 nm and M_s of SPIONs is varied from 20 to 90 emu/g. A2: Simulated harmonic ratios R35 for different SPION core sizes with identical M_s = 50 emu/g as a function of the excitation-field frequency. A3: Measured harmonic ratios R35 from SHP25, SMG30-I and -II, and MACS SPION samples as a function of the excitation-field frequency. A4: Measured phase lags at the third harmonic as a function of the excitation-field frequency. A5: Measured field-dependent harmonic amplitudes at f = 1 kHz with varying amplitudes. A6: Measured field-dependent dynamic M−H curves acquired at f = 1 kHz with varying amplitudes. (B) Three-point phantom. (C) Reconstructed images of the three-point phantom acquired during a single Lissajous sequence. (a−c) Reconstruction attempts using the individual SFs for Resovist, MM4, and MM4 powder, respectively. (d−f) Reconstruction of the three different materials into different images using combined SFs, which assign most of the signal to the correct sample. (g) Color overlay of the three images in parts d−f, where each image is assigned to one color channel. (A1−A4) Reprinted with permission from ref 66. Copyright 2017 Wiley. (A5 and A6) Reprinted with permission from ref 17. Copyright 2019 American Chemical Society. (B and C) From ref 119; licensed under CC BY 3.0.

research groups reporting the methods of simultaneous MPI and temperature/viscosity mapping using multi-SPION contrasts. In these studies, MPI provides SPION distribution images with high temporal and spatial resolution; meanwhile,

https://dx.doi.org/10.1021/acsanm.0c00890
ACS Appl. Nano Mater. 2020, 3, 4972−4989

the temperature/viscosity information is also separated from the MPS spectra. In 2016, Stehning et al. reported simultaneous MPI and temperature imaging using a multicolor reconstruction approach.[64] The proof of principle for the experimental setup is shown in Figure 5B. Two SPION samples (one supplied with tempered distilled water and the other with a nontempered reference) were mounted on a plastic hose at 15 mm. The reconstructed SPION amounts from both samples with the same size, C_{REF} and C_{TEMP}, were equivalent. The temperature signal of the nontempered reference SPION sample, T_{REF}, remained constant over the imaging experiment. The temperature signal of the tempered SPION sample, T_{TEMP}, declined as the circulating water temperature was lowered, as shown in Figure 5C. Furthermore, the spatially resolved MPI and temperature mappings are depicted in Figure 5D. The initial frames acquired at 37 °C are shown in the upper row, while the final frames acquired after the circulation of water when the tempered sample is at 12 °C are shown in the lower row. The color-coded subtraction images in Figure 5D (e and f) represent the temperature map. This method may allow for real-time temperature monitoring in image-guided interventions, such as interstitial hyperthermia, following the direct injection of nanoparticles. Later Möddel et al. reported a viscosity quantification method using multicontrast MPI.[22]

In 2014, Zhong et al. reported a new approach for a high-accuracy, remote temperature probing method by measuring the magnetization curves of SPIONs, where the theoretical models and inverse temperature calculations are described in ref 113. In 2016, Xu et al. reported a noninvasive, nanosecond-resolved temperature measurement using SPIONs with a nominal particle diameter of 10 nm (EMG 1300M, Ferrotec, Tokyo, Japan).[114] This method is based on the instantaneous change of the magnetic susceptibilities of SPIONs under a transient change in temperature. It was shown that temperature measurement can also be conducted on the SPION powders in addition to SPIONs dispersed in an aqueous medium. This design could be potentially applied for rapid acquisition of the internal temperature of materials in the industry and biomedical laser applications. Later in 2019, Guo et al. extended this method for remote temperature measurement from SPIONs in metal containers, extending the applicability of SPIONs from a nonmagnetic medium to a magnetic medium. Achieving an accuracy of 2 K in the temperature range of 320 to 400 K.[115] Zhong et al. reported a temperature imaging platform using SPIONs and a scanning MPS system, which shows great potential for noninvasive, in vivo temperature imaging beneath the surface of objects.[116] In their work, a system consisting of a mechanical scanner and a MPS was reported to measure the spatial distribution of the fundamental frequency f and the third harmonic 3f from SPIONs. Temperature imaging on a phantom with different temperature profiles was carried out, and a spatial resolution of 3.5 mm and a temperature resolution of 1 K were achieved.

Because both the temperature and viscosity modulate the magnetic responses of SPIONs, measuring one of these two parameters requires special attention to control (or remove) the effect of the other parameter. Elrefai et al. investigated the effects of viscosity on the harmonic signals of SPIONs for thermometry applications. In this work, they proposed a method to accurately estimate both the viscosity and temperature of a SPION sample even when the viscosity is unknown in advance, allowing for precise thermometry.[117]

3.2. MPS for Mechanical Force Monitoring. Wintzheimer et al. reported the application of MPS and SPIONs as sensors for mechanical stress.[65] The as-assembled SPIONs yield hollow microballoons (as shown in Figure 6A). This kind of structure is continuously fragmented when subjected to mechanical forces. By using MPS spectra, this structure deformation can be readily detected and enables quantification of the applied mechanical forces in ball mills. Parts B and C of Figure 6 depict the MPS harmonic amplitudes of the microballoons after the application of quasi-static compression or dynamic shear and impact forces, respectively. In both cases, the relative amplitude intensities drop with increasing mechanical energy, which proves that the MPS spectra of these hollow microballoon supraparticles are clearly distinguishable in the course of mechanical forces. This type of mechanical force sensor does not necessarily have to be removed from the processed material for measurements; furthermore, its magnetic property allows for easy removal after milling.

4. OTHER APPLICATIONS

4.1. MPS for SPION Characterization. As the sinusoidal magnetic fields excite SPIONs into their nonlinear saturation magnetization, the dynamic magnetic responses, represented by higher harmonics in the frequency domain, provide information about the physical and magnetic properties of the SPIONs. It has been reported that harmonic ratio R35 is inversely proportional to the saturation magnetization M_s and magnetic core diameter D of the SPION.[17,66,109,118] The harmonic phase angle (lag) of the magnetic moment to the excitation field carries the information on the hydrodynamic size of SPION. Numerical simulations were carried out to reveal the correlation between the harmonic ratio and M_s as well as D. As shown in Figure 7A (A1 and A2), a SPION system is assumed, with a log-normal size distribution, the effective anisotropy constant $K_{eff} = 1.8 \times 10^5$ erg/cm^3 (1.8×10^4 J/m^3), and M_s and D varied. The results show that, for SPIONs with identical core sizes, a smaller harmonic ratio R35 corresponds to higher M_s, while for SPIONs with identical M_s, a smaller core size yields a larger harmonic ratio R35. This conclusion is further proven by experimentally measuring the harmonic ratios from four commercially available SPION samples, as shown in Figure 7A (A3). For the SMG30-I and -II samples, with identical magnetic core size, a smaller harmonic ratio R35 from SMG30-II indicates a higher M_s over SMG30-I, which is further proven by the vibrating-sample magnetometry (VSM) results and high-angle annular dark-field scanning transmission electron microscopy−energy-dispersive X-ray spectroscopy mapping images.[66] In addition, the third harmonic phase lag to the excitation field recorded in Figure 7A (A4) shows that SMG30-I and -II SPIONs have similar hydrodynamic sizes and are larger than SHP25. On the other hand, for the multicore MACS SPIONs, the SPIONs are embedded in a polymer and the Néel process is dominating, which is a different scenario compared to those of single-core SPIONs (SHP25 and SMG30-I and -II).

In addition to the magnetic and physical properties of SPIONs that affect the MPS spectra (harmonic amplitudes and phases), the excitation fields should also be taken into consideration. Draack et al. reported the field-dependent MPS spectra by measuring SPIONs under different exaction field amplitudes and frequencies.[17] The field-dependent harmonic amplitudes are measured at a constant excitation

https://dx.doi.org/10.1021/acsanm.0c00890
ACS Appl. Nano Mater. 2020, 3, 4972−4989

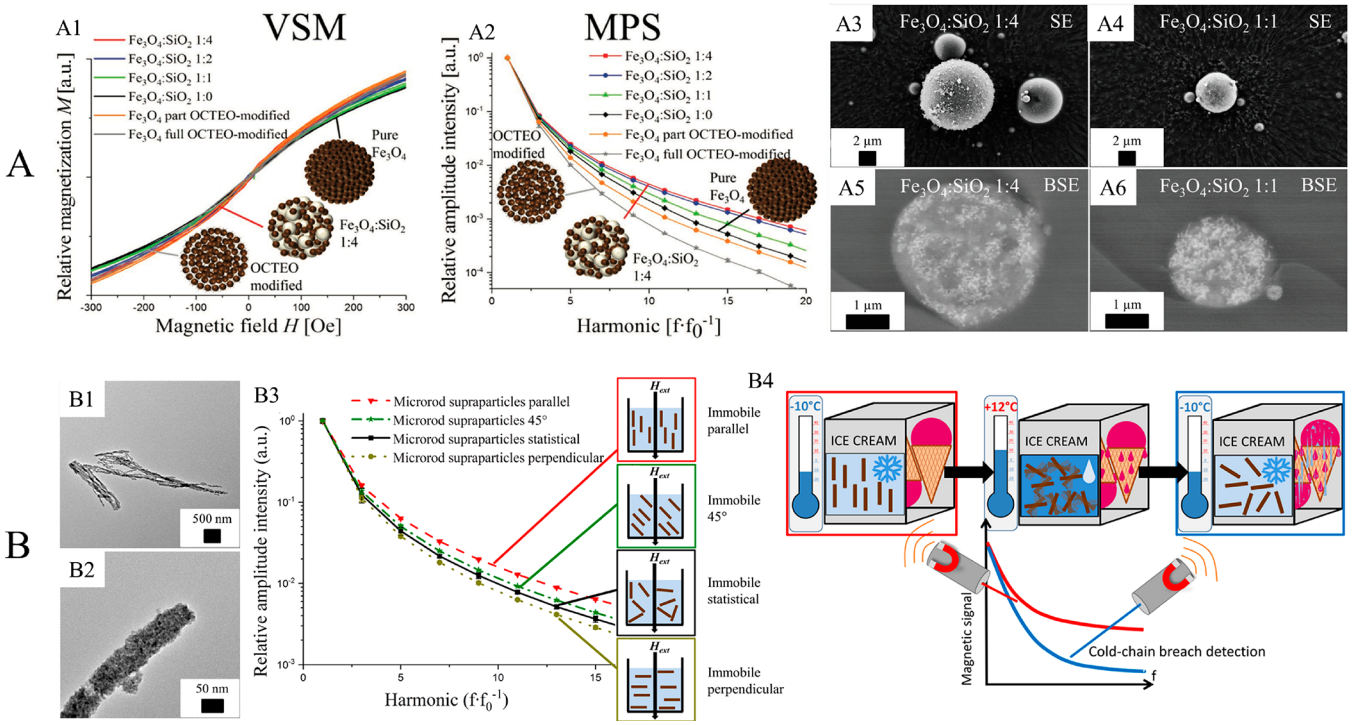

Figure 8. (A) A1: Normalized VSM magnetization curves of different supraparticles. A2: Relative amplitude intensity as a function of the higher harmonics of the same samples measured via MPS. A3 and A4: SEM images of supraparticles consisting of SPIONs and SiO_2 nanoparticles in weight ratios of 1:4 and 1:1. A5 and A6: Backscattered electron detector images visualizing the material contrast between the bright SPIONs and darker SiO_2 nanoparticles in the supraparticles with weight ratios of 1:4 and 1:1. (B) B1 and B2: TEM images of anisotropic microrod supraparticle morphologies. B3: MPS spectra of immobilized anisotropic microrods differently oriented with respect to the external excitation field. B4: Schematic depiction of ice cream packages equipped with a microrod-supraparticle-based temperature indicator. (A) Reprinted with permission from ref 67. Copyright 2019 Wiley. (B) Reprinted with permission from ref 68. Copyright 2019 American Chemical Society.

frequency, f = 1 kHz, with varying amplitudes from 5 to 25 mT, as shown in Figure 7A (A5). The dynamic $M-H$ curves are plotted in Figure 7A (A6). A higher magnetic field strength results in more saturated magnetization and a more pronounced hysteresis of the magnetization loops.

4.2. MPS for Magnetic Fingerprints. On the basis of the aforementioned phenomenon, each type of SPION with different magnetic core size D, hydrodynamic size, and saturation magnetization M_s shows unique MPS spectra, which could be used as magnetic fingerprints for target tracking and identification. Tu et al. reported a MPS method for the simultaneous characterization of two kinds of SPIONs with 20 and 35 nm core sizes.[39] The magnetic responses of each kind of SPION are recorded in both time and frequency domains. Then, the magnetic spectrum of each SPION is defined as the complex magnetization of the SPION. A phasor theory is proposed to allow for the quantification of each kind of SPION mixed at different ratios in solution. This study can potentially serve as a method for future magnetic multicolor labeling. In addition, Rahmer et al. reported a multicolor MPI, in which they experimentally demonstrated the ability to separate MPI signals from different types of SPIONs.[119] A reconstruction approach is proposed to reconstruct separate images for different SPIONs, which is combined into a single color-coded image. As shown in Figure 7B, a simple phantom is assembled by combining three kinds of SPIONs: 0.8 μL of undiluted Resovist [22 μg(Fe)], 3.1 μL of undiluted MM4 [9 μg(Fe)], and about 0.8 μL of dried MM4 powder [45 μg(Fe)]. The cylindrical cavities with diameters of 1, 1, and 2 mm are drilled for Resovist, MM4 powder, and fluid MM4 SPIONs. For experiments, all three SPIONs are measured simultaneously, whereas one of three is removed at a time so that only pairs of SPIONs are scanned simultaneously. Parts a–c of Figure 7C show the system functions (SFs) of each SPION material, and parts d–f of Figure 7C show two SPION material reconstructions by concatenation of three individual SFs. A color overlay of parts d–f of Figure 7C is displayed in Figure 7C (g). This multicolor MPI design could be very useful for many applications in the fields of medical imaging and therapy.

Müssig et al. reported the specially engineered magnetic supraparticles that exhibit a unique magnetic signature in MPS, proving its potential for marker applications.[67] In their work, the supraparticles are formed by assembling SPIONs with SiO_2 nanoparticles with different ratios, as shown in Figure 8A (A3–A6). They prepared different kinds of supraparticles by mixing SPIONs (~10 nm) and SiO_2 nanoparticles (~20 nm) in weight ratios of 1:0, 1:1, 1:2, and 1:4. The $M-H$ curves measured by VSM are plotted in Figure 8A (A1), yet the differences with respect to hysteresis loops can hardly be quantified. However, clearly distinguishable MPS spectra are observed in Figure 8A (A2). In contrast to VSM, MPS spectra of various supraparticles are easily quantified by determining the amplitudes of higher harmonics. In addition to mixing SPIONs with nonmagnetic SiO_2 nanoparticles, changing the interparticle distance by surface modification of SPIONs with OCTEO can also modify the MPS spectra [as shown in Figure 8A (A1 and A2), the "Fe_3O_4 part/full OCTEO-modified" curves]. This work shows that such supraparticles along with MPS could enable easy and versatile tracking and identification for products. By the mixing of different amounts of SiO_2

https://dx.doi.org/10.1021/acsanm.0c00890
ACS Appl. Nano Mater. 2020, 3, 4972–4989

Table 1. Summary on MPS-Based Applications

application	SPION (d_{core})	driving field	assay time	analyte	matrix	ref
immunoassay	d_{core}~ 30 nm	17 mT, 500 Hz to 20 kHz; 1.7 mT, 10 Hz	10 s	streptavidin	PBS buffer[a]	31
	d_{core}~ 50 nm	10 mT, 290−2110 Hz	5 s	thrombin	PBS buffer	19
	d_{core}~ 30 nm	17 mT, 500 Hz to 20 kHz; 1.7 mT, 10 Hz	10 s	H1N1 NP	PBS buffer	38
	SPIONs of 30 nm embedded in a 200 nm glycidyl methacrylate polymer bead (poly-GMA)	4 mT, 330 Hz		CRP	PBS buffer	79
	hydrodynamic size ~ 160 nm	4 mT, 1 kHz		CRP	HEPES buffer[b] serum buffer	78
monitor cellular uptake	Feraheme (d_{core} ~ 5 nm), CD021110 (d_{core} ~ 4 nm)	25 mT, 25 kHz		tumor cell lines (HeLa and Jurkat)	cell culture medium	35
	d_{core} ~ 7 nm	25 mT, 25 kHz		THP-1 cells	cell culture medium	50
cell vitality assessment		20 mT, 20 kHz		hMSCs	cell culture medium	51
monitor particle uptake and transport at cellular barriers	hydrodynamic size ~ 140 nm	25 mT, 25 kHz		HBMEC	cell culture medium	37
viscosity monitoring	$CoFe_2O_4$, d_{core} = 15.5 nm	25 mT, 500 Hz			water−glycerol mixtures	17
	d_{core} = 25 nm	10 mT, 15 kHz; 1 mT, 50 Hz	1.5 min		human serum	23
simultaneous MPI and temperature mapping						64
temperature measurement	d_{core} = 10 nm	35 kA/m (44 mT), dc field	14.4 ns		air	114
	d_{core} = 15 nm	10 mT, 1495 Hz			PBS buffer	116
simultaneous temperature and viscosity measurement	d_{core} = 30 nm, hydrodynamic size = 60 nm	3 mT, 10 kHz			PBS buffer	117
mechanical force monitoring	~40 μm hollow microballoon supraparticle assembled from SPIONs	30 mT, 20.1 kHz				65
SPION characterization	SHP25 (d_{core} ~ 25 nm), SMG30-I (d_{core} ~ 30 nm), SMG30-II (d_{core} ~ 30 nm), MACS (multicore, hydrodynamic size ~ 50 nm)	10 mT, 8−22 kHz; 1 mT, 50 Hz			PBS buffer	66
	$CoFe_2O_4$, d_{core} = 15.5 nm	5−25 mT, 1 kHz				17
magnetic fingerprints	SPIONs of ~10 nm and SiO_2 of ~10 nm are mixed and spray dried	30 mT, 20 kHz				67
	microrods assembled from SPIONs of ~10 nm.	30 mT, 20.1 kHz				68
determine the total circulating blood volume	FeraSpin R (nanoPET Pharma GmbH, Berlin, Germany)	20 mT, 20 kHz			rat blood	69
evaluate blood clot progression	d_{core} ~ 50 nm, hydrodynamic size = 116 nm	10 mT, 400−1600 Hz			pig blood	18
	d_{core} ~ 25 nm, hydrodynamic size = 40 nm	10 mT, 25 kHz	30 s		human blood	70

[a]Phosphate-buffered saline buffer. [b]4-(2-Hydroxyethyl)-1-piperazineethanesulfonic acid (HEPES) buffer.

https://dx.doi.org/10.1021/acsanm.0c00890
ACS Appl. Nano Mater. 2020, 3, 4972−4989

Table 2. Comparison of Different Nanoparticle-Based Biosensing Platforms with MPS

technology	nanoparticle	target analyte	detection limit	matrix	ref
MPS	SPION	H1N1 NP	4.4 nM	PBS buffer	38
	SPION	CRP	20.6 ng/mL	PBS buffer	78
	SPION	thrombin	4 nM	PBS buffer	19
	SPION	Cardiac troponin I	0.01 ng/mL	native blood sample	120
	SPION	BoNT types A, B, and E	0.11−0.32 ng/mL	PBS buffer	90
GMR	SPIONs encapsulated in the polymer matrix	H1N1 NP	15 ng/mL	PBS buffer	121
	SPIONs encapsulated in the polymer matrix	H1N1 and H3N2 virus	250 $TCID_{50}$/ml	swine nasal swab sample	122
	SPIONs encapsulated in the polymer matrix	human chorionic gonadotropin	1 pM	blood serum	123
MTJ	SPIONs encapsulated in polymer matrix	ssDNA	5 nM	PBS buffer	124
QD[a]	cadmium−tellurium quantum dots	human T-lymphotropic virus-1	19.5 pg/μL	tris-borate buffer	125
	glutathione-capped CdTe quantum dots	protamine	1 ng/mL	human blood plasma	126
	CdS and PbS nanocrystal tracers	thrombin	0.5 pM	acetate buffer	127
SERS[b]	plasmonic gold nanostar	bilirubin	0.436 μM	blood serum	128
	gold nanoparticles	Staphylococcal enterotoxin B	0.001 ng/mL	buffer solution	129
	gold nanoparticles	4-mercatopyridine	1 nM	DI water	130
	gold nanoparticles	*S. aureus*	10^3 cfu/ml	spinach wash	131
	500 nm magnetic beads	TSST	1 pg/mL	PBS buffer	99
NMR[c]	SPION	Dengue virus (DENV) NS1 protein	2 pg/μL	serum	132
	SPION	circulating tumor cells (CTCs)	∼3 individual CTCs per sample (1−10 mL blood)	whole blood	133
	SPION	*L. monocytogenes*	3 MPN	milk powder and lettuce	134
	Fe-NFPs@PEG	H1N1 NP	100 ng/mL	PBS buffer	135
	SPION	Microcystin-LR (MC-LR)	0.6 ng/mL	lake water	136

[a]Quantum dot. [b]Surface-enhanced Raman spectroscopy. [c]Nuclear magnetic resonance.

nanoparticles with SPIONs or structural adjustment of the SPIONs, it is possible to change the magnetic properties (MPS spectra) of supraparticles and generate countless unique magnetic fingerprints.

Microrods assembled from SPIONs have also been reported as magnetic fingerprints because the orientation-dependent MPS spectral variations of anisotropic microrods are identifiable, as shown in Figure 8B (B1−B3).[68] When the microrod supraparticles are oriented parallel and perpendicular with respect to the excitation field, the MPS spectra with the highest and lowest intensities are observed, respectively. Figure 8B (B4) schematically depicted the ice cream packages equipped with a microrod-supraparticle-based temperature indicator. The initially aligned and frozen microrod supraparticles become mobile when an undesired temperature increase melts the frozen matrix. The refreezing of the matrix immobilizes the microrod supraparticles in a different alignment and thus makes a potential quality loss detectable by their respective MPS curves. This unique property of anisotropic supraparticles enables the detection of cold-chain breaches (e.g., during delivery of a product that needs to be cooled all of the time) simply by recording the initial and final MPS spectra of microrod supraparticles integrated in the container of a frozen product.

4.3. MPS-Based Blood Analysis. Determining the patient's total blood volume is an essential topic in clinical routine. A variety of methods are reported, but because of the extended volume and dispersion throughout the body, a direct measurement seems unfeasible. A promising approach to determining the total circulating blood volume is based on the dilution measurement of applied tracers. Fidler et al. reported a MPS method along with SPION tracers for this purpose.[69] They used FeraSpin R SPIONs with a hydrodynamic diameter of 60 nm and a blood half-life in rat of 15 min. However, for a prolonged blood half-life, another product FeraSpin XS with a hydrodynamic diameter of 15 nm and a blood half-life in rat of 30 min is also recommended. This method consists of three major steps: First, estimate the undiluted SPION tracer and choose a specific volume of injection. Second, inject the SPION sample into the subject. Third, draw a small amount of blood after a mixing time. From the measured concentration, the total circulating blood volume is calculated.

Another work reported by Hafsa et al. proposed the evaluation of blood clot progression using SPION tracers and MPS.[18] By measurement of the SPIONs' relaxation time in the clot vicinity, the clot age, clot stiffness, and amount of SPIONs bound to the clot could be estimated. It was reported that, during the clot formation, SPIONs become trapped in the clot mesh, which restricts their Brownian relaxation process, causing an increase of their relaxation time.[70] In this work, SPIONs are surface-functionalized with ATP15 and ATP29 aptamers, which bind to heteroepitopes on thrombin. SPIONs bound to thrombi are identified by their increased relaxation time using MPS. Harmonic ratio R35 is reported as the metric for the Brownian process, which, in turn, reflects the bound state of SPIONs.

5. CONCLUSION

In this review, we summarized the recent advances in MPS-based applications, which are shown in Table 1. For biological

https://dx.doi.org/10.1021/acsanm.0c00890
ACS Appl. Nano Mater. 2020, 3, 4972−4989

and biomedical assays, by surface functionalization of suitable ligands/antibodies/aptamers/proteins on SPIONs that could specifically bind to target analytes, SPIONs are explored as magnetic markers, and their dynamic magnetic responses are monitored by MPS. The binding events of target analytes affect the Brownian process and dynamic magnetic responses of SPIONs and cause detectable changes in the harmonic amplitudes, phases, and harmonic ratios. Because of the negligible magnetic background from biological samples, highly sensitive detection could be achieved by using SPIONs as biomarkers. This detection mechanism based on a MPS platform allows simple, fast, inexpensive, and high-sensitivity bioassays. Compared to other sensing platforms where SPIONs are used as contrasts/markers/tracers, MPS is a volume-based sensing system in which the magnetic signal directly comes from the whole medium (a biological sample or a nonmagnetic medium) where the SPIONs locate. This allows for one-step, easy-to-use, and wash-free detection of dynamic magnetic responses from SPIONs for different assay purposes. Surface-based sensing platforms such as magnetoresistive [e.g., giant magnetoresistive (GMR), magnetic tunnel junction (MTJ), anisotropic magnetoresistive] and Hall sensors require the highly demanded nano- or macrofabrication of sensors and, in addition, detectable signals only from SPIONs that are in the proximity of sensor surfaces. The comparisons of MPS with other sensing platforms that use SPIONs as contrasts/markers/tracers have recently been reviewed in ref 2. In Table 2, we compared different biosensing platforms that use nanoparticles (magnetic and nonmagnetic) for the detection of protein biomarkers, viruses, pathogens, nucleic acids, etc.

In the areas of cell labeling, tracking, and cell-based theragnostics (therapy and diagnostics), MPS provides a quantitative method to evaluate the SPION (or iron) content from contrast biological matrixes and even in living cells. Upon the interaction with biological materials such as cells, SPIONs undergo physicochemical changes that alter their MPS spectra. In addition to these standalone applications, MPS has also developed into a mature auxiliary tool supporting the magnetic imaging and hyperthermia by providing real-time, high spatial and temporal resolution viscosity/temperature mapping. Other applications based on MPS such as SPION characterizations, magnetic fingerprints, and blood analysis are also reviewed.

In summary, many good works have been reported in recent years based on the MPS platform, and this process is still ongoing. With the unique nonlinear magnetic responses of SPIONs, facile surface chemical modifications, and flexible structural design of SPION assemblies (supraparticles) with superior magnetic/physical properties, MPS has found its position in increasingly new areas.

AUTHOR INFORMATION

Corresponding Authors

Kai Wu − *Department of Electrical and Computer Engineering, University of Minnesota, Minneapolis, Minnesota 55455, United States;* orcid.org/0000-0002-9444-6112; Email: wuxx0803@umn.edu

Jian-Ping Wang − *Department of Electrical and Computer Engineering, University of Minnesota, Minneapolis, Minnesota 55455, United States;* orcid.org/0000-0003-2815-6624; Email: jpwang@umn.edu

Authors

Diqing Su − *Department of Chemical Engineering and Material Science, University of Minnesota, Minneapolis, Minnesota 55455, United States;* orcid.org/0000-0002-5790-8744

Renata Saha − *Department of Electrical and Computer Engineering, University of Minnesota, Minneapolis, Minnesota 55455, United States;* orcid.org/0000-0002-0389-0083

Jinming Liu − *Department of Electrical and Computer Engineering, University of Minnesota, Minneapolis, Minnesota 55455, United States;* orcid.org/0000-0002-4313-5816

Vinit Kumar Chugh − *Department of Electrical and Computer Engineering, University of Minnesota, Minneapolis, Minnesota 55455, United States*

Complete contact information is available at: https://pubs.acs.org/10.1021/acsanm.0c00890

Notes

The authors declare no competing financial interest.

ACKNOWLEDGMENTS

This study was financially supported by the Institute of Engineering in Medicine of the University of Minnesota through the FY18 IEM Seed Grant Funding Program, a Distinguished McKnight University Professorship, a Centennial Chair Professorship, and a Robert F, Hartmann Endowed Chair from the University of Minnesota.

REFERENCES

(1) Liu, J.; Su, D.; Wu, K.; Wang, J.-P. High-Moment Magnetic Nanoparticles. *J. Nanopart. Res.* **2020**, *22* (3), 1−16.

(2) Wu, K.; Su, D.; Liu, J.; Saha, R.; Wang, J.-P. Magnetic Nanoparticles in Nanomedicine: A Review of Recent Advances. *Nanotechnology* **2019**, *30* (50), 502003.

(3) Liu, J.; Schliep, K.; He, S.-H.; Ma, B.; Jing, Y.; Flannigan, D. J.; Wang, J.-P. Iron Nanoparticles with Tunable Tetragonal Structure and Magnetic Properties. *Phys. Rev. Mater.* **2018**, *2* (5), 054415.

(4) Srinoi, P.; Chen, Y.-T.; Vittur, V.; Marquez, M. D.; Lee, T. R. Bimetallic Nanoparticles: Enhanced Magnetic and Optical Properties for Emerging Biological Applications. *Appl. Sci.* **2018**, *8* (7), 1106.

(5) Li, Y.; Wang, N.; Huang, X.; Li, F.; Davis, T. P.; Qiao, R.; Ling, D. Polymer-Assisted Magnetic Nanoparticle Assemblies for Biomedical Applications. *ACS Appl. Bio Mater.* **2020**, *3*, 121.

(6) Mora, B.; Perez-Valle, A.; Redondo, C.; Boyano, M. D.; Morales, R. Cost-Effective Design of High-Magnetic Moment Nanostructures for Biotechnological Applications. *ACS Appl. Mater. Interfaces* **2018**, *10* (9), 8165−8172.

(7) Liu, J.; Wu, K.; Wang, J.-P. Magnetic Properties of Cubic FeCo Nanoparticles with Anisotropic Long Chain Structure. *AIP Adv.* **2016**, *6* (5), No. 056126.

(8) Yew, Y. P.; Shameli, K.; Miyake, M.; Ahmad Khairudin, N. B. E.; Mohamad, S. E. B.; Naiki, T.; Lee, K. X. Green Biosynthesis of Superparamagnetic Magnetite Fe3O4 Nanoparticles and Biomedical Applications in Targeted Anticancer Drug Delivery System: A Review. *Arabian J. Chem.* **2020**, *13* (1), 2287−2308.

(9) Biederer, S.; Knopp, T.; Sattel, T.; Lüdtke-Buzug, K.; Gleich, B.; Weizenecker, J.; Borgert, J.; Buzug, T. Magnetization Response Spectroscopy of Superparamagnetic Nanoparticles for Magnetic Particle Imaging. *J. Phys. D: Appl. Phys.* **2009**, *42*, 205007.

(10) Arami, H.; Khandhar, A. P.; Tomitaka, A.; Yu, E.; Goodwill, P. W.; Conolly, S. M.; Krishnan, K. M. In Vivo Multimodal Magnetic Particle Imaging (MPI) with Tailored Magneto/Optical Contrast Agents. *Biomaterials* **2015**, *52*, 251−261.

(11) Dhavalikar, R.; Rinaldi, C. On the Effect of Finite Magnetic Relaxation on the Magnetic Particle Imaging Performance of Magnetic Nanoparticles. *J. Appl. Phys.* **2014**, *115* (7), No. 074308.

(12) Gleich, B.; Weizenecker, J. Tomographic Imaging Using the Nonlinear Response of Magnetic Particles. *Nature* **2005**, *435* (7046), 1214−1217.
(13) Deissler, R. J.; Martens, M. A. Dependence of the Magnetization Response on the Driving Field Amplitude for Magnetic Particle Imaging and Spectroscopy. *IEEE Trans. Magn.* **2015**, *51*, 1−4.
(14) Du, Y.; Lai, P. T.; Leung, C. H.; Pong, P. W. Design of Superparamagnetic Nanoparticles for Magnetic Particle Imaging (MPI). *Int. J. Mol. Sci.* **2013**, *14* (9), 18682−18710.
(15) Paysen, H.; Loewa, N.; Weber, K.; Kosch, O.; Wells, J.; Schaeffter, T.; Wiekhorst, F. Imaging and Quantification of Magnetic Nanoparticles: Comparison of Magnetic Resonance Imaging and Magnetic Particle Imaging. *J. Magn. Magn. Mater.* **2019**, *475*, 382−388.
(16) Wu, K.; Su, D.; Saha, R.; Wong, D.; Wang, J.-P. Magnetic Particle Spectroscopy-Based Bioassays: Methods, Applications, Advances, and Future Opportunities. *J. Phys. D: Appl. Phys.* **2019**, *52*, 173001.
(17) Draack, S.; Lucht, N.; Remmer, H.; Martens, M.; Fischer, B.; Schilling, M.; Ludwig, F.; Viereck, T. Multiparametric Magnetic Particle Spectroscopy of CoFe2O4 Nanoparticles in Viscous Media. *J. Phys. Chem. C* **2019**, *123* (11), 6787−6801.
(18) Khurshid, H.; Shi, Y.; Berwin, B. L.; Weaver, J. B. Evaluating Blood Clot Progression Using Magnetic Particle Spectroscopy. *Med. Phys.* **2018**, *45* (7), 3258−3263.
(19) Zhang, X.; Reeves, D. B.; Perreard, I. M.; Kett, W. C.; Griswold, K. E.; Gimi, B.; Weaver, J. B. Molecular Sensing with Magnetic Nanoparticles Using Magnetic Spectroscopy of Nanoparticle Brownian Motion. *Biosens. Bioelectron.* **2013**, *50*, 441−446.
(20) Paysen, H.; Wells, J.; Kosch, O.; Steinhoff, U.; Trahms, L.; Schaeffter, T.; Wiekhorst, F. Towards Quantitative Magnetic Particle Imaging: A Comparison with Magnetic Particle Spectroscopy. *AIP Adv.* **2018**, *8* (5), No. 056712.
(21) Yu, K.; Zhang, M.; Li, Y.; Wang, R. Increased Whole Blood Viscosity Associated with Arterial Stiffness in Patients with Non-alcoholic Fatty Liver Disease. *J. Gastroenterol. Hepatol.* **2014**, *29* (3), 540−544.
(22) Möddel, M.; Meins, C.; Dieckhoff, J.; Knopp, T. Viscosity Quantification Using Multi-Contrast Magnetic Particle Imaging. *New J. Phys.* **2018**, *20* (8), No. 083001.
(23) Wu, K.; Liu, J.; Wang, Y.; Ye, C.; Feng, Y.; Wang, J.-P. Superparamagnetic Nanoparticle-Based Viscosity Test. *Appl. Phys. Lett.* **2015**, *107*, No. 053701.
(24) Wu, K.; Ye, C.; Liu, J.; Wang, Y.; Feng, Y.; Wang, J.-P. Vitro Viscosity Measurement on Superparamagnetic Nanoparticle Suspensions. *IEEE Trans. Magn.* **2016**, *52* (7), 1.
(25) Draack, S.; Viereck, T.; Kuhlmann, C.; Schilling, M.; Ludwig, F.. Temperature-Dependent MPS Measurements. *Int. J. Magn. Part. Imaging* **2017**, *3* (1).
(26) Perreard, I.; Reeves, D.; Zhang, X.; Kuehlert, E.; Forauer, E.; Weaver, J. Temperature of the Magnetic Nanoparticle Microenvironment: Estimation from Relaxation Times. *Phys. Med. Biol.* **2014**, *59*, 1109.
(27) Weaver, J. B.; Rauwerdink, A. M.; Hansen, E. W. Magnetic Nanoparticle Temperature Estimation. *Med. Phys.* **2009**, *36* (5), 1822−1829.
(28) Wells, J.; Paysen, H.; Kosch, O.; Trahms, L.; Wiekhorst, F. Temperature Dependence in Magnetic Particle Imaging. *AIP Adv.* **2018**, *8* (5), No. 056703.
(29) Orlov, A. V.; Bragina, V. A.; Nikitin, M. P.; Nikitin, P. I. Rapid Dry-Reagent Immunomagnetic Biosensing Platform Based on Volumetric Detection of Nanoparticles on 3D Structures. *Biosens. Bioelectron.* **2016**, *79*, 423−429.
(30) Nikitin, M. P.; Orlov, A.; Sokolov, I.; Minakov, A.; Nikitin, P.; Ding, J.; Bader, S.; Rozhkova, E.; Novosad, V. Ultrasensitive Detection Enabled by Nonlinear Magnetization of Nanomagnetic Labels. *Nanoscale* **2018**, *10* (24), 11642−11650.
(31) Wu, K.; Liu, J.; Su, D.; Saha, R.; Wang, J.-P. Magnetic Nanoparticle Relaxation Dynamics-Based Magnetic Particle Spectroscopy for Rapid and Wash-Free Molecular Sensing. *ACS Appl. Mater. Interfaces* **2019**, *11* (26), 22979−22986.
(32) Shah, S. A.; Reeves, D. B.; Ferguson, R. M.; Weaver, J. B.; Krishnan, K. M. Mixed Brownian Alignment and Néel Rotations in Superparamagnetic Iron Oxide Nanoparticle Suspensions Driven by an Ac Field. *Phys. Rev. B: Condens. Matter Mater. Phys.* **2015**, *92* (9), No. 094438.
(33) Weaver, J. B.; Harding, M.; Rauwerdink, A. M.; Hansen, E. W. The Effect of Viscosity on the Phase of the Nanoparticle Magnetization Induced by a Harmonic Applied Field; *Proc. SPIE*, **2010**762627−762628.
(34) Shi, Y.; Jyoti, D.; Gordon-Wylie, S. W.; Weaver, J. B. Quantification of Magnetic Nanoparticles by Compensating for Multiple Environment Changes Simultaneously. *Nanoscale* **2020**, *12* (1), 195−200.
(35) Loewa, N.; Wiekhorst, F.; Gemeinhardt, I.; Ebert, M.; Schnorr, J.; Wagner, S.; Taupitz, M.; Trahms, L. Cellular Uptake of Magnetic Nanoparticles Quantified by Magnetic Particle Spectroscopy. *IEEE Trans. Magn.* **2013**, *49* (1), 275−278.
(36) Löwa, N.; Seidel, M.; Radon, P.; Wiekhorst, F. Magnetic Nanoparticles in Different Biological Environments Analyzed by Magnetic Particle Spectroscopy. *J. Magn. Magn. Mater.* **2017**, *427*, 133−138.
(37) Gräfe, C.; Slabu, I.; Wiekhorst, F.; Bergemann, C.; von Eggeling, F.; Hochhaus, A.; Trahms, L.; Clement, J. H. Magnetic Particle Spectroscopy Allows Precise Quantification of Nanoparticles after Passage through Human Brain Microvascular Endothelial Cells. *Phys. Med. Biol.* **2016**, *61* (11), 3986.
(38) Wu, K.; Liu, J.; Saha, R.; Su, D.; Krishna, V. D.; Cheeran, M. C.-J.; Wang, J.-P. Magnetic Particle Spectroscopy for Detection of Influenza A Virus Subtype H1N1. *ACS Appl. Mater. Interfaces* **2020**, *12* (12), 13686−13697.
(39) Tu, L.; Wu, K.; Klein, T.; Wang, J.-P. Magnetic Nanoparticles Colourization by a Mixing-Frequency Method. *J. Phys. D: Appl. Phys.* **2014**, *47*, 155001.
(40) Bragina, V. A.; Znoyko, S. L.; Orlov, A. V.; Pushkarev, A. V.; Nikitin, M. P.; Nikitin, P. I. Analytical Platform with Selectable Assay Parameters Based on Three Functions of Magnetic Nanoparticles: Demonstration of Highly Sensitive Rapid Quantitation of Staphylococcal Enterotoxin B in Food. *Anal. Chem.* **2019**, *91* (15), 9852−9857.
(41) Znoyko, S. L.; Orlov, A. V.; Pushkarev, A. V.; Mochalova, E. N.; Guteneva, N. V.; Lunin, A. V.; Nikitin, M. P.; Nikitin, P. I. Ultrasensitive Quantitative Detection of Small Molecules with Rapid Lateral-Flow Assay Based on High-Affinity Bifunctional Ligand and Magnetic Nanolabels. *Anal. Chim. Acta* **2018**, *1034*, 161−167.
(42) Wu, K.; Su, D.; Saha, R.; Liu, J.; Wang, J.-P. Investigating the Effect of Magnetic Dipole−Dipole Interaction on Magnetic Particle Spectroscopy: Implications for Magnetic Nanoparticle-Based Bioassays and Magnetic Particle Imaging. *J. Phys. D: Appl. Phys.* **2019**, *52* (33), 335002.
(43) Van De Loosdrecht, M. M.; Draack, S.; Waanders, S.; Schlief, J. G. L.; Krooshoop, H. J. G.; Viereck, T.; Ludwig, F.; Ten Haken, B. A Novel Characterization Technique for Superparamagnetic Iron Oxide Nanoparticles: The Superparamagnetic Quantifier, Compared with Magnetic Particle Spectroscopy. *Rev. Sci. Instrum.* **2019**, *90* (2), No. 024101.
(44) Hong, C.-Y.; Wu, C.; Chiu, Y.; Yang, S.-Y.; Horng, H.-E.; Yang, H.-C. Magnetic Susceptibility Reduction Method for Magnetically Labeled Immunoassay. *Appl. Phys. Lett.* **2006**, *88*, 212512.
(45) Yang, C.; Yang, S.-Y.; Chen, H.; Weng, W.; Horng, H.-E.; Chieh, J.-J.; Hong, C.; Yang, H.-C. Effect of Molecule-Particle Binding on the Reduction in the Mixed-Frequency Alternating Current Magnetic Susceptibility of Magnetic Bio-Reagents. *J. Appl. Phys.* **2012**, *112*, No. 024704.
(46) Hong, C.-Y.; Chen, W.; Jian, Z.; Yang, S.-Y.; Horng, H.-E.; Yang, L.; Yang, H.-C. Wash-Free Immunomagnetic Detection for Serum through Magnetic Susceptibility Reduction. *Appl. Phys. Lett.* **2007**, *90*, No. 074105.

https://dx.doi.org/10.1021/acsanm.0c00890
ACS Appl. Nano Mater. 2020, 3, 4972−4989

(47) Rauwerdink, A. M.; Weaver, J. B. Harmonic Phase Angle as a Concentration-Independent Measure of Nanoparticle Dynamics. *Med. Phys.* **2010**, *37*, 2587−2592.
(48) Tu, L.; Jing, Y.; Li, Y.; Wang, J.-P. Real-Time Measurement of Brownian Relaxation of Magnetic Nanoparticles by a Mixing-Frequency Method. *Appl. Phys. Lett.* **2011**, *98*, 213702.
(49) Wawrzik, T.; Schilling, M.; Ludwig, F. Perspectives of Magnetic Particle Spectroscopy for Magnetic Nanoparticle Characterization. *Magnetic Particle Imaging*; Springer, 2012; pp 41−45.
(50) Poller, W. C.; Löwa, N.; Wiekhorst, F.; Taupitz, M.; Wagner, S.; Möller, K.; Baumann, G.; Stangl, V.; Trahms, L.; Ludwig, A. Magnetic Particle Spectroscopy Reveals Dynamic Changes in the Magnetic Behavior of Very Small Superparamagnetic Iron Oxide Nanoparticles during Cellular Uptake and Enables Determination of Cell-Labeling Efficacy. *J. Biomed. Nanotechnol.* **2016**, *12* (2), 337−346.
(51) Fidler, F.; Steinke, M.; Kraupner, A.; Grüttner, C.; Hiller, K.-H.; Briel, A.; Westphal, F.; Walles, H.; Jakob, P. M. Stem Cell Vitality Assessment Using Magnetic Particle Spectroscopy. *IEEE Trans. Magn.* **2015**, *51* (2), 1−4.
(52) Im, S. H.; Herricks, T.; Lee, Y. T.; Xia, Y. Synthesis and Characterization of Monodisperse Silica Colloids Loaded with Superparamagnetic Iron Oxide Nanoparticles. *Chem. Phys. Lett.* **2005**, *401* (1−3), 19−23.
(53) Yi, D. K.; Selvan, S. T.; Lee, S. S.; Papaefthymiou, G. C.; Kundaliya, D.; Ying, J. Y. Silica-Coated Nanocomposites of Magnetic Nanoparticles and Quantum Dots. *J. Am. Chem. Soc.* **2005**, *127* (14), 4990−4991.
(54) Burke, B. P.; Baghdadi, N.; Clemente, G. S.; Camus, N.; Guillou, A.; Kownacka, A. E.; Domarkas, J.; Halime, Z.; Tripier, R.; Archibald, S. J. Final Step Gallium-68 Radiolabelling of Silica-Coated Iron Oxide Nanorods as Potential PET/MR Multimodal Imaging Agents. *Faraday Discuss.* **2014**, *175*, 59−71.
(55) Selvan, S. T.; Patra, P. K.; Ang, C. Y.; Ying, J. Y. Synthesis of Silica-coated Semiconductor and Magnetic Quantum Dots and Their Use in the Imaging of Live Cells. *Angew. Chem., Int. Ed.* **2007**, *46* (14), 2448−2452.
(56) Yen, S. K.; Padmanabhan, P.; Selvan, S. T. Multifunctional Iron Oxide Nanoparticles for Diagnostics, Therapy and Macromolecule Delivery. *Theranostics* **2013**, *3* (12), 986.
(57) Alwi, R.; Telenkov, S.; Mandelis, A.; Leshuk, T.; Gu, F.; Oladepo, S.; Michaelian, K. Silica-Coated Super Paramagnetic Iron Oxide Nanoparticles (SPION) as Biocompatible Contrast Agent in Biomedical Photoacoustics. *Biomed. Opt. Express* **2012**, *3* (10), 2500−2509.
(58) Yen, S. K.; Varma, D. P.; Guo, W. M.; Ho, V. H.; Vijayaragavan, V.; Padmanabhan, P.; Bhakoo, K.; Selvan, S. T. Synthesis of Small-Sized, Porous, and Low-Toxic Magnetite Nanoparticles by Thin POSS Silica Coating. *Chem. - Eur. J.* **2015**, *21* (10), 3914−3918.
(59) Lee, H.; Lee, E.; Kim, D. K.; Jang, N. K.; Jeong, Y. Y.; Jon, S. Antibiofouling Polymer-Coated Superparamagnetic Iron Oxide Nanoparticles as Potential Magnetic Resonance Contrast Agents for in Vivo Cancer Imaging. *J. Am. Chem. Soc.* **2006**, *128* (22), 7383−7389.
(60) Yen, S. K.; Janczewski, D.; Lakshmi, J. L.; Dolmanan, S. B.; Tripathy, S.; Ho, V. H.; Vijayaragavan, V.; Hariharan, A.; Padmanabhan, P.; Bhakoo, K. K.; et al. Design and Synthesis of Polymer-Functionalized NIR Fluorescent Dyes−Magnetic Nanoparticles for Bioimaging. *ACS Nano* **2013**, *7* (8), 6796−6805.
(61) Zhang, F.; Lees, E.; Amin, F.; Rivera-Gil, P.; Yang, F.; Mulvaney, P.; Parak, W. J. Polymer-coated Nanoparticles: A Universal Tool for Biolabelling Experiments. *Small* **2011**, *7* (22), 3113−3127.
(62) Unterweger, H.; Dézsi, L.; Matuszak, J.; Janko, C.; Poettler, M.; Jordan, J.; Bäuerle, T.; Szebeni, J.; Fey, T.; Boccaccini, A. R.; Alexiou, C.; Cicha, I. Dextran-Coated Superparamagnetic Iron Oxide Nanoparticles for Magnetic Resonance Imaging: Evaluation of Size-Dependent Imaging Properties, Storage Stability and Safety. *Int. J. Nanomed.* **2018**, *13*, 1899.
(63) Basiruddin, S. K.; Ranjan Maity, A.; Jana, N. R. Glucose/Galactose/Dextran-Functionalized Quantum Dots, Iron Oxide and Doped Semiconductor Nanoparticles With< 100 Nm Hydrodynamic Diameter. *RSC Adv.* **2012**, *2* (31), 11915−11921.
(64) Stehning, C.; Gleich, B.; Rahmer, J. Simultaneous Magnetic Particle Imaging (MPI) and Temperature Mapping Using Multi-Color MPI. *Int. J. Magn. Part. Imaging* **2016**, *2* (2).
(65) Wintzheimer, S.; Müssig, S.; Wenderoth, S.; Prieschl, J.; Granath, T.; Fidler, F.; Haddad, D.; Mandel, K. Hollow Superparamagnetic Nanoparticle-Based Microballoons for Mechanical Force Monitoring by Magnetic Particle Spectroscopy. *ACS Appl. Nano Mater.* **2019**, *2* (10), 6757−6762.
(66) Wu, K.; Schliep, K.; Zhang, X.; Liu, J.; Ma, B.; Wang, J. Characterizing Physical Properties of Superparamagnetic Nanoparticles in Liquid Phase Using Brownian Relaxation. *Small* **2017**, *13*, 1604135.
(67) Müssig, S.; Fidler, F.; Haddad, D.; Hiller, K.-H.; Wintzheimer, S.; Mandel, K. Supraparticles with a Magnetic Fingerprint Readable by Magnetic Particle Spectroscopy: An Alternative beyond Optical Tracers. *Adv. Mater. Technol.* **2019**, *4* (9), 1900300.
(68) Müssig, S.; Granath, T.; Schembri, T.; Fidler, F.; Haddad, D.; Hiller, K.-H.; Wintzheimer, S.; Mandel, K. Anisotropic Magnetic Supraparticles with a Magnetic Particle Spectroscopy Fingerprint as Indicators for Cold-Chain Breach. *ACS Appl. Nano Mater.* **2019**, *2* (8), 4698−4702.
(69) Weigl, F.; Seifert, A.; Kraupner, A.; Jakob, P. M.; Hiller, K.-H.; Fidler, F. Determination of the Total Circulating Blood Volume Using Magnetic Particle Spectroscopy. *Int. J. Magn. Part. Imaging* **2017**, *3* (1).
(70) Starmans, L. W.; Moonen, R. P.; Aussems-Custers, E.; Daemen, M. J.; Strijkers, G. J.; Nicolay, K.; Grüll, H. Evaluation of Iron Oxide Nanoparticle Micelles for Magnetic Particle Imaging (MPI) of Thrombosis. *PLoS One* **2015**, *10* (3), e0119257.
(71) Sasayama, T.; Yoshida, T.; Enpuku, K. Relationship between Harmonic Spectra and Coercive Field of Immobilized Magnetic Nanoparticles. *Jpn. J. Appl. Phys.* **2017**, *56* (2), No. 025001.
(72) Yoshida, T.; Sasayama, T.; Enpuku, K. Effect of Core Size Distribution of Immobilized Magnetic Nanoparticles on Harmonic Magnetization. *Int. J. Magn. Part. Imaging* **2017**, *3* (1).
(73) Ota, S.; Matsugi, Y.; Nakamura, T.; Takeda, R.; Takemura, Y.; Kato, I.; Nohara, S.; Sasayama, T.; Yoshida, T.; Enpuku, K. Effects of Size and Anisotropy of Magnetic Nanoparticles Associated with Dynamics of Easy Axis for Magnetic Particle Imaging. *J. Magn. Magn. Mater.* **2019**, *474*, 311−318.
(74) Yoshida, T.; Matsugi, Y.; Tsujimura, N.; Sasayama, T.; Enpuku, K.; Viereck, T.; Schilling, M.; Ludwig, F. Effect of Alignment of Easy Axes on Dynamic Magnetization of Immobilized Magnetic Nanoparticles. *J. Magn. Magn. Mater.* **2017**, *427*, 162−167.
(75) Elrefai, A. L.; Yoshida, T.; Enpuku, K. Magnetic Parameters Evaluation of Magnetic Nanoparticles for Use in Biomedical Applications. *J. Magn. Magn. Mater.* **2019**, *474*, 522−527.
(76) Kuhlmann, C.; Khandhar, A. P.; Ferguson, R. M.; Kemp, S.; Wawrzik, T.; Schilling, M.; Krishnan, K. M.; Ludwig, F. Drive-Field Frequency Dependent MPI Performance of Single-Core Magnetite Nanoparticle Tracers. *IEEE Trans. Magn.* **2015**, *51* (2), 1−4.
(77) Viereck, T.; Kuhlmann, C.; Draack, S.; Schilling, M.; Ludwig, F. Dual-Frequency Magnetic Particle Imaging of the Brownian Particle Contribution. *J. Magn. Magn. Mater.* **2017**, *427*, 156−161.
(78) Enpuku, K.; Shibakura, M.; Arao, Y.; Mizoguchi, T.; Kandori, A.; Hara, M.; Tsukada, K. Wash-Free Detection of C-Reactive Protein Based on Third-Harmonic Signal Measurement of Magnetic Markers. *Jpn. J. Appl. Phys.* **2018**, *57* (9), No. 090309.
(79) Akiyoshi, K.; Yoshida, T.; Sasayama, T.; Elrefai, A. L.; Hara, M.; Enpuku, K. Wash-Free Detection of Biological Target Using Cluster Formation of Magnetic Markers. *J. Magn. Magn. Mater.* **2020**, *500*, 166356.
(80) Cascella, M.; Rajnik, M.; Cuomo, A.; Dulebohn, S. C.; Di Napoli, R. Features, Evaluation and Treatment Coronavirus (COVID-19). *Statpearls [internet]*; StatPearls Publishing, 2020.

https://dx.doi.org/10.1021/acsanm.0c00890
ACS Appl. Nano Mater. 2020, 3, 4972−4989

(81) Mehta, P.; McAuley, D. F.; Brown, M.; Sanchez, E.; Tattersall, R. S.; Manson, J. J. COVID-19: Consider Cytokine Storm Syndromes and Immunosuppression. *Lancet* **2020**, *395* (10229), 1033−1034.
(82) World Health Organization. *Coronavirus Disease 2019 (COVID-19): Situation Report 70*, 2020.
(83) World Health Organization. *Coronavirus Disease 2019 (COVID-19): Situation Report 72*, 2020.
(84) Xu, Z.; Shi, L.; Wang, Y.; Zhang, J.; Huang, L.; Zhang, C.; Liu, S.; Zhao, P.; Liu, H.; Zhu, L.; et al. Pathological Findings of COVID-19 Associated with Acute Respiratory Distress Syndrome. *Lancet Respir. Med.* **2020**, *8* (4), 420−422.
(85) Emanuel, E. J.; Persad, G.; Upshur, R.; Thome, B.; Parker, M.; Glickman, A.; Zhang, C.; Boyle, C.; Smith, M.; Phillips, J. P. *Fair Allocation of Scarce Medical Resources in the Time of Covid-19*; Mass Medical Society, 2020.
(86) Fang, Y.; Zhang, H.; Xie, J.; Lin, M.; Ying, L.; Pang, P.; Ji, W. Sensitivity of Chest CT for COVID-19: Comparison to RT-PCR. *Radiology* **2020**, 200432.
(87) Lan, L.; Xu, D.; Ye, G.; Xia, C.; Wang, S.; Li, Y.; Xu, H. Positive RT-PCR Test Results in Patients Recovered from COVID-19. *Jama* **2020**, *323* (15), 1502−1503.
(88) Chan, J. F.-W.; Yip, C. C.-Y.; To, K. K.-W.; Tang, T. H.-C.; Wong, S. C.-Y.; Leung, K.-H.; Fung, A. Y.-F.; Ng, A. C.-K.; Zou, Z.; Tsoi, H.-W.et al. Improved Molecular Diagnosis of COVID-19 by the Novel, Highly Sensitive and Specific COVID-19-RdRp/Hel Real-Time Reverse Transcription-PCR Assay Validated in Vitro and with Clinical Specimens. *J. Clin. Microbiol.*. **2020**, *58* (5). DOI: 10.1128/JCM.00310-20
(89) Yang, W.; Yan, F. Patients with RT-PCR Confirmed COVID-19 and Normal Chest CT. *Radiology* **2020**, *295*, 200702.
(90) Orlov, A. V.; Znoyko, S. L.; Cherkasov, V. R.; Nikitin, M. P.; Nikitin, P. I. Multiplex Biosensing Based on Highly Sensitive Magnetic Nanolabel Quantification: Rapid Detection of Botulinum Neurotoxins A, B, and E in Liquids. *Anal. Chem.* **2016**, *88* (21), 10419−10426.
(91) Chen, Y.; Xianyu, Y.; Wang, Y.; Zhang, X.; Cha, R.; Sun, J.; Jiang, X. One-Step Detection of Pathogens and Viruses: Combining Magnetic Relaxation Switching and Magnetic Separation. *ACS Nano* **2015**, *9* (3), 3184−3191.
(92) Gong, J.-L.; Liang, Y.; Huang, Y.; Chen, J.-W.; Jiang, J.-H.; Shen, G.-L.; Yu, R.-Q. Ag/SiO 2 Core-Shell Nanoparticle-Based Surface-Enhanced Raman Probes for Immunoassay of Cancer Marker Using Silica-Coated Magnetic Nanoparticles as Separation Tools. *Biosens. Bioelectron.* **2007**, *22* (7), 1501−1507.
(93) Herrmann, I.; Schlegel, A.; Graf, R.; Stark, W. J.; Beck-Schimmer, B. Magnetic Separation-Based Blood Purification: A Promising New Approach for the Removal of Disease-Causing Compounds? *J. Nanobiotechnol.* **2015**, *13* (1), 49.
(94) He, J.; Huang, M.; Wang, D.; Zhang, Z.; Li, G. Magnetic Separation Techniques in Sample Preparation for Biological Analysis: A Review. *J. Pharm. Biomed. Anal.* **2014**, *101*, 84−101.
(95) Hola, K.; Markova, Z.; Zoppellaro, G.; Tucek, J.; Zboril, R. Tailored Functionalization of Iron Oxide Nanoparticles for MRI, Drug Delivery, Magnetic Separation and Immobilization of Biosubstances. *Biotechnol. Adv.* **2015**, *33* (6), 1162−1176.
(96) Inglis, D. W.; Riehn, R.; Austin, R.; Sturm, J. Continuous Microfluidic Immunomagnetic Cell Separation. *Appl. Phys. Lett.* **2004**, *85* (21), 5093−5095.
(97) Iranmanesh, M.; Hulliger, J. Magnetic Separation: Its Application in Mining, Waste Purification, Medicine, Biochemistry and Chemistry. *Chem. Soc. Rev.* **2017**, *46* (19), 5925−5934.
(98) Tamer, U.; Boyaci, I. H.; Temur, E.; Zengin, A.; Dincer, I.; Elerman, Y. Fabrication of Magnetic Gold Nanorod Particles for Immunomagnetic Separation and SERS Application. *J. Nanopart. Res.* **2011**, *13* (8), 3167−3176.
(99) Yang, K.; Hu, Y.; Dong, N. A Novel Biosensor Based on Competitive SERS Immunoassay and Magnetic Separation for Accurate and Sensitive Detection of Chloramphenicol. *Biosens. Bioelectron.* **2016**, *80*, 373−377.
(100) Huang, J.; Bu, L.; Xie, J.; Chen, K.; Cheng, Z.; Li, X.; Chen, X. Effects of Nanoparticle Size on Cellular Uptake and Liver MRI with Polyvinylpyrrolidone-Coated Iron Oxide Nanoparticles. *ACS Nano* **2010**, *4* (12), 7151−7160.
(101) Saritas, E. U.; Goodwill, P. W.; Croft, L. R.; Konkle, J. J.; Lu, K.; Zheng, B.; Conolly, S. M. Magnetic Particle Imaging (MPI) for NMR and MRI Researchers. *J. Magn. Reson.* **2013**, *229*, 116−126.
(102) Wang, Y.-X. J. Superparamagnetic Iron Oxide Based MRI Contrast Agents: Current Status of Clinical Application. *Quant. Imaging Med. Surg.* **2011**, *1* (1), 35.
(103) Löwa, N.; Radon, P..; Kosch, O.; Wiekhorst, F. Concentration Dependent MPI Tracer Performance. *Int. J. Magn. Part. Imaging* **2016**, *2* (1).
(104) Zanganeh, S.; Aieneravaie, M.; Erfanzadeh, M.; Ho, J.; Spitler, R. Magnetic Particle Imaging (MPI). In *Iron Oxide Nanoparticles for Biomedical Applications*; Elsevier, 2018; pp 115−133.
(105) Boutry, S.; Forge, D.; Burtea, C.; Mahieu, I.; Murariu, O.; Laurent, S.; Vander Elst, L.; Muller, R. N. How to Quantify Iron in an Aqueous or Biological Matrix: A Technical Note. *Contrast Media Mol. Imaging* **2009**, *4* (6), 299−304.
(106) Maxwell, D. J.; Bonde, J.; Hess, D. A.; Hohm, S. A.; Lahey, R.; Zhou, P.; Creer, M. H.; Piwnica-Worms, D.; Nolta, J. A. Fluorophore-conjugated Iron Oxide Nanoparticle Labeling and Analysis of Engrafting Human Hematopoietic Stem Cells. *Stem Cells* **2008**, *26* (2), 517−524.
(107) Luo, X. F.; Xie, X. Q.; Cheng, S.; Yang, Y.; Yan, J.; Zhang, H.; Chai, W. M.; Schmidt, B.; Yan, F. H. Dual-Energy CT for Patients Suspected of Having Liver Iron Overload: Can Virtual Iron Content Imaging Accurately Quantify Liver Iron Content? *Radiology* **2015**, *277* (1), 95−103.
(108) Riemer, J.; Hoepken, H. H.; Czerwinska, H.; Robinson, S. R.; Dringen, R. Colorimetric Ferrozine-Based Assay for the Quantitation of Iron in Cultured Cells. *Anal. Biochem.* **2004**, *331* (2), 370−375.
(109) Wu, K.; Tu, L.; Su, D.; Wang, J.-P. Magnetic Dynamics of Ferrofluids: Mathematical Models and Experimental Investigations. *J. Phys. D: Appl. Phys.* **2017**, *50* (8), No. 085005.
(110) Utkur, M.; Muslu, Y.; Saritas, E. U. Relaxation-Based Viscosity Mapping for Magnetic Particle Imaging. *Phys. Med. Biol.* **2017**, *62* (9), 3422.
(111) Perreard, I.; Reeves, D.; Zhang, X.; Weaver, J. B. *Magnetic Nanoparticles Temperature Measurements*, 2013.
(112) Rauwerdink, A. M.; Hansen, E. W.; Weaver, J. B. Nanoparticle Temperature Estimation in Combined Ac and Dc Magnetic Fields. *Phys. Med. Biol.* **2009**, *54*, L51.
(113) Zhong, J.; Liu, W.; Kong, L.; Morais, P. C. A New Approach for Highly Accurate, Remote Temperature Probing Using Magnetic Nanoparticles. *Sci. Rep.* **2015**, *4*, 6338.
(114) Xu, W.; Liu, W.; Zhang, P. Nanosecond-Resolved Temperature Measurements Using Magnetic Nanoparticles. *Rev. Sci. Instrum.* **2016**, *87* (5), No. 054902.
(115) Guo, S.; Liu, W.; Cheng, J. A Penetrating Remote Temperature Measurement Device Based on Magnetic Nanoparticles for Measuring the Internal Temperatures of Metal Containers. *Meas. Sci. Technol.* **2019**, *30* (5), No. 055101.
(116) Zhong, J.; Schilling, M.; Ludwig, F. Magnetic Nanoparticle Temperature Imaging with a Scanning Magnetic Particle Spectrometer. *Meas. Sci. Technol.* **2018**, *29* (11), 115903.
(117) Elrefai, A. L.; Yoshida, T.; Enpuku, K. Effect of Viscosity on Harmonics Signals of Magnetic Nanoparticles for Thermometry Application. *J. Magn. Magn. Mater.* **2019**, *491*, 165480.
(118) Wu, K.; Su, D.; Liu, J.; Wang, J.-P. Estimating Saturation Magnetization of Superparamagnetic Nanoparticles in Liquid Phase. *J. Magn. Magn. Mater.* **2019**, *471*, 394−399.
(119) Rahmer, J.; Halkola, A.; Gleich, B.; Schmale, I.; Borgert, J. First Experimental Evidence of the Feasibility of Multi-Color Magnetic Particle Imaging. *Phys. Med. Biol.* **2015**, *60* (5), 1775.
(120) Nikitin, M.; Orlov, A.; Znoyko, S.; Bragina, V.; Gorshkov, B.; Ksenevich, T.; Cherkasov, V.; Nikitin, P. Multiplex Biosensing with

https://dx.doi.org/10.1021/acsanm.0c00890
ACS Appl. Nano Mater. 2020, 3, 4972−4989

Highly Sensitive Magnetic Nanoparticle Quantification Method. *J. Magn. Magn. Mater.* **2018**, *459*, 260−264.
(121) Wu, K.; Klein, T.; Krishna, V. D.; Su, D.; Perez, A. M.; Wang, J.-P. Portable GMR Handheld Platform for the Detection of Influenza A Virus. *ACS Sens.* **2017**, *2*, 1594−1601.
(122) Su, D.; Wu, K.; Krishna, V.; Klein, T.; Liu, J.; Feng, Y.; Perez, A. M.; Cheeran, M. C.; Wang, J.-P. Detection of Influenza a Virus in Swine Nasal Swab Samples With a Wash-Free Magnetic Bioassay and a Handheld Giant Magnetoresistance Sensing System. *Front. Microbiol.* **2019**, *10*, 1077.
(123) Osterfeld, S. J.; Yu, H.; Gaster, R. S.; Caramuta, S.; Xu, L.; Han, S.-J.; Hall, D. A.; Wilson, R. J.; Sun, S.; White, R. L.; et al. Multiplex Protein Assays Based on Real-Time Magnetic Nanotag Sensing. *Proc. Natl. Acad. Sci. U. S. A.* **2008**, *105* (52), 20637−20640.
(124) Grancharov, S. G.; Zeng, H.; Sun, S.; Wang, S. X.; O'Brien, S.; Murray, C.; Kirtley, J.; Held, G. Bio-Functionalization of Monodisperse Magnetic Nanoparticles and Their Use as Biomolecular Labels in a Magnetic Tunnel Junction Based Sensor. *J. Phys. Chem. B* **2005**, *109* (26), 13030−13035.
(125) Norouzi, M.; Zarei Ghobadi, M.; Golmimi, M.; Mozhgani, S.-H.; Ghourchian, H.; Rezaee, S. A. Quantum Dot-Based Biosensor for the Detection of Human T-Lymphotropic Virus-1. *Anal. Lett.* **2017**, *50* (15), 2402−2411.
(126) Ensafi, A. A.; Kazemifard, N.; Rezaei, B. A Simple and Rapid Label-Free Fluorimetric Biosensor for Protamine Detection Based on Glutathione-Capped CdTe Quantum Dots Aggregation. *Biosens. Bioelectron.* **2015**, *71*, 243−248.
(127) Hansen, J. A.; Wang, J.; Kawde, A.-N.; Xiang, Y.; Gothelf, K. V.; Collins, G. Quantum-Dot/Aptamer-Based Ultrasensitive Multi-Analyte Electrochemical Biosensor. *J. Am. Chem. Soc.* **2006**, *128* (7), 2228−2229.
(128) Pan, X.; Li, L.; Lin, H.; Tan, J.; Wang, H.; Liao, M.; Chen, C.; Shan, B.; Chen, Y.; Li, M. A Graphene Oxide-Gold Nanostar Hybrid Based-Paper Biosensor for Label-Free SERS Detection of Serum Bilirubin for Diagnosis of Jaundice. *Biosens. Bioelectron.* **2019**, *145*, 111713.
(129) Hwang, J.; Lee, S.; Choo, J. Application of a SERS-Based Lateral Flow Immunoassay Strip for the Rapid and Sensitive Detection of Staphylococcal Enterotoxin B. *Nanoscale* **2016**, *8* (22), 11418−11425.
(130) Zhang, L.; Xu, J. J.; Mi, L.; Gong, H.; Jiang, S. Y.; Yu, Q. M. Multifunctional Magnetic-Plasmonic Nanoparticles for Fast Concentration and Sensitive Detection of Bacteria Using SERS. *Biosens. Bioelectron.* **2012**, *31* (1), 130−136.
(131) Wang, Y. L.; Ravindranath, S.; Irudayaraj, J. Separation and Detection of Multiple Pathogens in a Food Matrix by Magnetic SERS Nanoprobes. *Anal. Bioanal. Chem.* **2011**, *399* (3), 1271−1278.
(132) Huber, S.; Min, C.; Staat, C.; Oh, J.; Castro, C. M.; Haase, A.; Weissleder, R.; Gleich, B.; Lee, H. Multichannel Digital Heteronuclear Magnetic Resonance Biosensor. *Biosens. Bioelectron.* **2019**, *126*, 240−248.
(133) Ghazani, A. A.; Castro, C. M.; Gorbatov, R.; Lee, H.; Weissleder, R. Sensitive and Direct Detection of Circulating Tumor Cells by Multimarker M-Nuclear Magnetic Resonance. *Neoplasia N. Y. NY* **2012**, *14* (5), 388.
(134) Zhao, Y.; Li, Y.; Jiang, K.; Wang, J.; White, W. L.; Yang, S.; Lu, J. Rapid Detection of Listeria Monocytogenes in Food by Biofunctionalized Magnetic Nanoparticle Based on Nuclear Magnetic Resonance. *Food Control* **2017**, *71*, 110−116.
(135) Jeun, M.; Park, S.; Lee, H.; Lee, K. H. Highly Sensitive Detection of Protein Biomarkers via Nuclear Magnetic Resonance Biosensor with Magnetically Engineered Nanoferrite Particles. *Int. J. Nanomed.* **2016**, *11*, 5497.
(136) Ma, W.; Chen, W.; Qiao, R.; Liu, C.; Yang, C.; Li, Z.; Xu, D.; Peng, C.; Jin, Z.; Xu, C.; Zhu, S.; Wang, L. Rapid and Sensitive Detection of Microcystin by Immunosensor Based on Nuclear Magnetic Resonance. *Biosens. Bioelectron.* **2009**, *25* (1), 240−243.

https://dx.doi.org/10.1021/acsanm.0c00890
ACS Appl. Nano Mater. 2020, 3, 4972−4989